

# Fracton Spin Liquid and Exotic Frustrated Phases in Ising-like Octochlore Magnets

Matthew Stern,<sup>1,\*</sup> Michael D. Burke,<sup>2,\*</sup> Michel J. P. Gingras,<sup>2,3</sup> Judit Romhányi,<sup>1</sup> and Kristian Tyn Kai Chung<sup>4,5</sup>

<sup>1</sup>*Department of Physics and Astronomy, University of California, Irvine, California 92697, USA*

<sup>2</sup>*Department of Physics and Astronomy, University of Waterloo, Waterloo, Ontario, N2L 3G1, Canada*

<sup>3</sup>*Waterloo Institute for Nanotechnology, University of Waterloo, Waterloo, Ontario, N2L 3G1, Canada*

<sup>4</sup>*Max Planck Institute for the Physics of Complex Systems, Nöthnitzer Strasse 38, 01187 Dresden, Germany*

<sup>5</sup>*Department of Physics and Astronomy, Rice University, Houston, Texas 77005, USA*

(Dated: March 16, 2026)

For nearly three decades frustrated magnetism research in three dimensions (3D) has centered on the pyrochlore geometry of corner-sharing tetrahedra and the classical spin liquid (CSL) known as spin ice. In this work, we propose that a lattice of corner-sharing octahedra—appropriately dubbed the octochlore lattice—may provide a next-generation platform for the study of 3D frustrated magnetism, with realizations in anti-perovskite and certain potassium-fluoride compounds. We study the phase diagram of Ising spins on the octochlore lattice with first- and second-neighbor interactions within each octahedron, which displays a rich variety of frustrated phases, including CSLs with extensive ground state degeneracies, as well as phases with subextensive ground state degeneracies intermediate between spin liquids and long-range order. In addition to a spin ice CSL, we identify a novel fracton CSL with excitations restricted to move along one-dimensional (1D) lines, which is a classical U(1) analog of the celebrated X-cube model, a paradigmatic realization of fracton topological order. The existence of these two CSLs is rationalized as condensation of 1D ferro-spinons bound states from a parent phase with subextensive degeneracy due to frustration of ferromagnetically polarized chains. We also find a spin nematic phase exhibiting two-stage dimensional reduction from cubic to tetragonal (uniaxial) and finally orthorhombic (biaxial) symmetry, driven by strong fluctuations arising from deconfined 1D antiferro-spinons. This work paves the way for the potential realization of fracton CSLs and the exploration of other exotic frustrated states in real materials.

## CONTENTS

I. Introduction	2	C. Fluctuation-Driven Biaxial Dimensional Reduction	16
II. Hamiltonian and Irreducible Multipoles	3	VII. Discussion	17
A. Irreducible Multipole Moments	4	A. Theoretical Outlook	18
B. Fragmentation of the $E_u$ Irrep	4	B. Materials and Experimental Outlook	18
III. Phase Diagram	5	C. Conclusion	19
A. Degeneracies and Flat Bands	5	Acknowledgments	19
B. Phase Boundaries	6	References	19
C. Phases	7	A. Conventions	22
IV. $T_{1g}$ Frustrated Chains Phase	8	B. Irreps and Multipoles	23
A. Chain Interactions via 1D Spinon Collisions	8	1. Irrep Decomposition of Spin Configurations	24
B. Low-Temperature Behavior	9	C. Interaction Matrices	24
C. Spin Liquids from Condensation of Spinon Bound States	10	D. Self-Consistent Gaussian Approximation	25
V. $T_{1g} \oplus A_{1u}$ Cage-Net Fracton Spin Liquid	10	E. Structure Factors and Neutron Scattering	25
A. Cage-Net Tunneling Between Ground States	11	F. Monte Carlo Simulations	26
B. Thermodynamics from Cluster Monte Carlo	12	1. Cluster Algorithm for the X-cube Fracton CSL	26
C. Rank-2 Tensor Spin Liquid: U(1) X-cube Model	12	2. Finite-Temperature Phase Diagram	27
D. Pinch Lines and Neutron Scattering Diagnostics	13	3. Thermodynamics	27
VI. $E_u \wedge A_{1u}$ Spin Nematic Phase	14	4. X-cube Spin Liquid	27
A. Two Transitions: Uniaxial and Biaxial Spin Nematics	14	5. Spin Nematic	28
B. Uniaxial Nematic Phase Transition	15		

\* These authors contributed equally to the project.

## I. INTRODUCTION

For the past thirty years, frustrated magnets have been a leading platform for the study of exotic condensed matter physics phenomena, with a rich interplay of theoretical and experimental developments [1]. Frustration, arising from competing spin-spin interactions, can significantly suppress the development of magnetic order, leaving systems paramagnetic well below their Curie temperatures. In this regime, strong correlations and quantum fluctuations can give rise to complex behaviors. In particular, they may stabilize a spin liquid state that hosts emergent deconfined gauge fields rather than conventional symmetry-breaking long-range order.

In three dimensions (3D), pyrochlore rare-earth magnets have become standard bearers of the field, which are naturally frustrated by tetrahedral coordination of magnetic ions, with the tetrahedra forming a corner-sharing network [2–5]. The interplay of strong spin-orbit coupling and crystalline electric field effects in these systems often results in Ising-like moments [2, 3]. The most famous examples are the compounds  $\text{Dy}_2\text{Ti}_2\text{O}_7$  [6–8] and  $\text{Ho}_2\text{Ti}_2\text{O}_7$  [9–12]. At low temperatures, these materials realize a classical spin liquid (CSL) called spin ice [13] governed at low temperatures by a local 2-in–2-out “ice rule” constraint of the four Ising moments on each tetrahedron, an emergent zero-divergence Gauss constraint, giving rise to fractionalized quasiparticle excitations behaving as magnetic monopoles [14–16].

Recent work has focused on exploring 3-component continuous-spin models on various frustrated lattices, which are readily amenable to “soft spin” coarse-grained descriptions in the classical large-spin limit, and for which CSLs arise from flat bands in the momentum-space spectrum of the spin-spin interaction matrix [17–20]. These studies have clarified that CSLs naturally arise at classical multicritical points where multiple ordered phases become degenerate [3, 21–27]. This strategy has led to the realization of numerous examples of so-called higher-rank CSLs [22–24, 28–30], whose emergent tensor Gauss laws are closely related to those of fracton gauge theories [31–33]. Such gauge theories locally conserve multipole moments, restricting the gauge charges to sub-dimensional mobility, either rendering them entirely immobile or confining their motion to lines or planes of the crystalline lattice [34]. However, continuous-spin classical liquids do not have discrete gapped quasiparticle excitations, so their fractonic nature can only be defined indirectly [35, 36]. Furthermore, there are no controlled and unbiased methods for determining the stability of continuous-spin CSLs as quantum models, i.e., to determine whether quantum fluctuations drive them towards quantum spin liquids (QSLs) or ordered ground states.

Classical Ising models, on the other hand, have clearly-defined gapped excitations, and correspond to the classical limit of a quantum spin-1/2 model wherein off-diagonal spin-flipping operators are absent from the Hamiltonian. As such, an Ising CSL can be promoted to a QSL by turning such spin flipping terms on, perturbatively generating “ring-exchange” terms which flip correlated clusters of spins, inducing quantum tunneling between classical ground states [3, 5, 37–39].

However, the low-temperature properties of highly frustrated classical 3D Ising models are much more challenging to expose compared to their continuous-spin counterparts. In particular, they are not well-approximated by soft spins, and require carefully tailored numerical methods to study. For this reason, they remain relatively unstudied beyond pyrochlore spin ice [38].

For the purpose of understanding the full breadth of frustrated Ising moments and expanding the experimental discovery of novel quantum materials, the pyrochlore Ising model, notwithstanding its eminence, offers in retrospect limited options. As a tetrahedron supports only nearest-neighbor Ising spin-spin couplings, the pyrochlore’s network of corner-sharing tetrahedra can only exhibit two phases: either 2-in–2-out spin ice or all-in–all-out (AIAO) order [40, 41]. In this work, we advance the understanding of frustrated 3D Ising models by focusing on a different lattice—a network of corner-sharing *octahedra*, appropriately dubbed the *octochlore lattice*, depicted in Fig. 1(a). From a materials perspective, the octochlore geometry is realized by the magnetic-moment-bearing M sites of anti-perovskite (or inverse-perovskite) compounds with chemical formula  $\text{M}_3\text{AX}$  [42–47], and also in a class of magnetic trivalent rare-earth (R) fluoride insulators of chemical formula  $\text{AR}_3\text{F}_{10}$  [48–54]. We provide a more detailed overview of these materials in the Discussion (Section VII). Among lattices of corner-sharing clusters [55, 56], the octochlore lattice is the logical next step “up” from the pyrochlore lattice—going from a four-coordinated cluster (tetrahedron) to a six-coordinated one (octahedron). This extension naturally provides new quadrupolar (nematic) degrees of freedom, in addition to the monopole (AIAO) and dipole (spin ice) ones. Correspondingly, the octochlore lattice affords an extra tuning parameter in the form of a second-neighbor coupling *within* the elementary frustrated octahedral unit, in contrast to the single energy scale for an individual tetrahedron in the pyrochlore lattice.

Previous works studying octochlore spin models focused on either isotropic Heisenberg models [57, 58] or spin ice physics [37, 43], leaving the broader Ising phase diagram largely unexplored. In this work we study the complete phase diagram of the intra-octahedral couplings in detail. We do this by leveraging intuition gained from years of study of spin ice physics, along with the more recent insights afforded by the tools of irreducible representation (irrep) analysis [21–23, 29] and highly efficient cluster Monte Carlo methods [59]. The irrep analysis (Section II) decomposes spin configurations on each octahedron into multipole contributions [22], and the additional degrees of freedom of the octahedral unit give rise to quadrupolar configurations, not achievable on the tetrahedron, which underpins the comparative richness of this model. The full phase diagram (Section III) is shown in Figure 1(f).

Remarkably, in addition to the spin ice point and an AIAO phase, we discover a classical Ising fracton CSL (Section V)—to the best of our knowledge, this is the first thus far reported in 3D (see Refs. [60, 61] for 2D models). We identify this as a U(1) CSL analog of the celebrated X-cube model, a paradigmatic realization of fracton topological order [62]. Whereas the excitations of spin ice are, famously, magnetic monopoles [15, 16], the excitations of the fracton CSL are

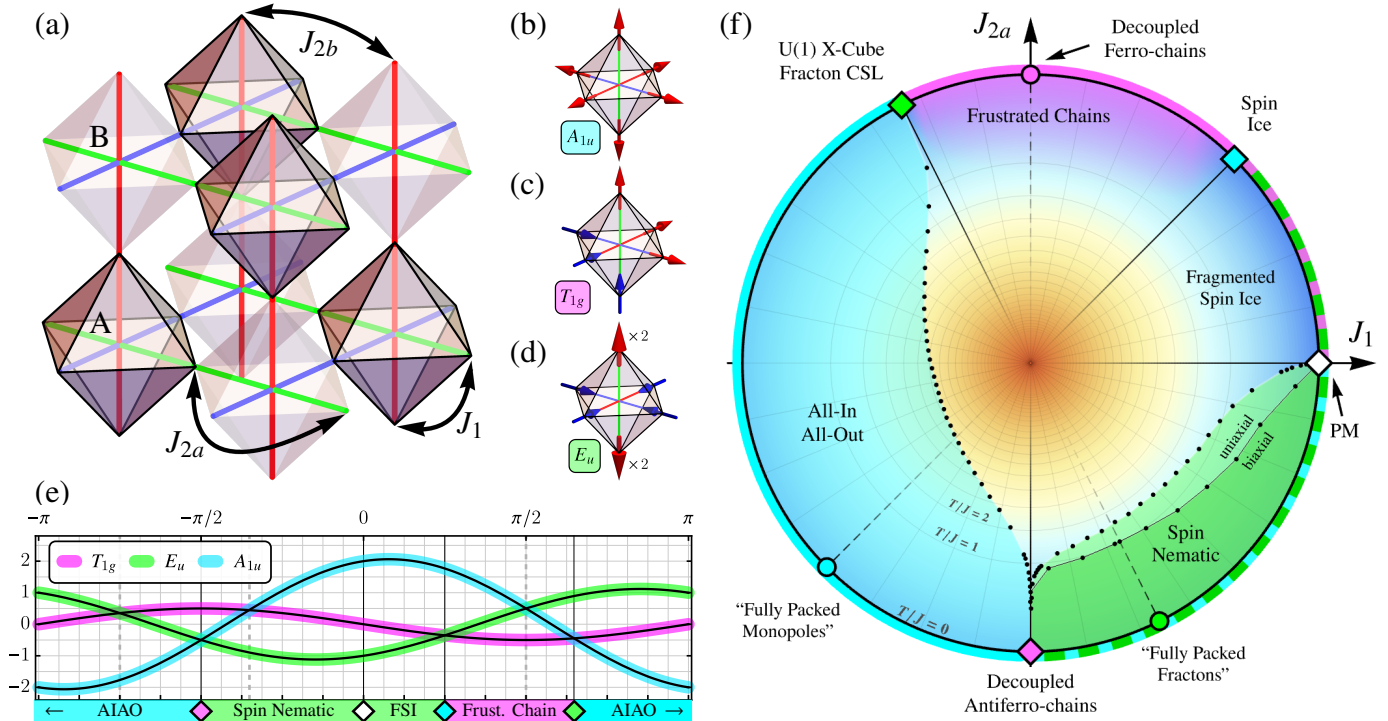


**FIG. 1. Overview of the octochlore Ising system.** (a) Octochlore lattice with first ( $J_1$ ) and second ( $J_{2a}$  and  $J_{2b}$ ) neighbor interactions. Octahedron centers form a bipartite simple cubic lattice; one “A” and one “B” octahedron are marked. Orthogonal 1D chains are illustrated with red, blue, and green colors. (b,c,d) The Ising moment configurations can be decomposed into multipole contributions—monopole ( $A_{1u}$ ), dipole ( $T_{1g}$ ), and quadrupole ( $E_u$ ) moments—which transform as irreducible representations (irreps) of the octahedral point group symmetry. Note that the  $E_u$  irrep is inconsistent with the fixed moment constraint  $|S_i^z| = 1$ , as indicated by doubled moment size ( $\times 2$ ) in panel (d). (e) Variation of irrep energies from Eq. (6) as a function of  $\theta$ , with the parameterization  $J_1 = J \cos(\theta)$  and  $J_{2a} = J \sin(\theta)$ . (f) Finite-temperature phase diagram of Eq. (1) as the function of  $\theta$  and temperature, with zero temperature at the outer edge and infinite temperature at the center. Black dots mark thermal phase transition critical temperatures obtained from Monte Carlo simulation Appendix F. The radial temperature scale is given by  $r(T) = 1 - \tanh \sqrt{T/10J} \in [0, 1]$ , with  $T = 0$  at the outer edge, increasing towards the center. A linear temperature scale version is provided in Appendix F.

identified as magnetic quadrupoles, which are restricted to move along straight lines. We identify the generalization of spin ice’s zero-energy loop moves [63] as “cage moves”, thus characterizing this CSL as a cage-net liquid [64] rather than a string-net liquid [65]. We develop a highly efficient cluster Monte Carlo algorithm generalizing one originally designed for spin ice [59] to explore this CSL down to zero temperature. Rather than pinch points [56], we identify the spectral signatures of this CSL as pinch lines [28, 30].

In addition to the U(1) X-cube fracton CSL, we identify two highly frustrated phases exhibiting subextensive ground state degeneracies, intermediate between spin liquids and conventional ordered phases. First, we find a phase whose ground states are independently polarized ferromagnetic chains hosting deconfined 1D spinons, with inter-chain interactions mediated by collisions of spinons moving on intersecting chains. We dub this the frustrated chains phase (Section IV). We show that this phase may be viewed as a “precursor” to both the spin ice and fracton CSLs, which can be viewed as condensates of 1D spinon bound states. Second, we find a phase exhibiting both uniaxial and biaxial spin nematic ordering (Section VI)—at a higher temperature the system spontaneously breaks cubic to tetragonal symmetry, stabilizing a uniaxial nematic liquid,

while at a lower temperature the system further breaks symmetry to orthorhombic, developing biaxial order. Analogous to how the AIAO phase is a maximal packing of the monopole charges of spin ice [66], the nematic phase can be viewed as a maximal packing of the fractonic excitations of the fracton CSL. We demonstrate that the biaxial transition is driven by a fluctuation mechanism similar to order-by-disorder, where the biaxial configurations support deconfined 1D antiferro-spinons, maximizing entropy at finite temperature.

## II. HAMILTONIAN AND IRREDUCIBLE MULTIPOLES

The octochlore lattice, depicted in Fig. 1(a), is a network of corner-sharing octahedra. It is the line graph (or medial lattice) of the bipartite simple cubic lattice [56], meaning that vertices of the octochlore lattice correspond to edge-centers of the cubic lattice, and vertices of the cubic lattice correspond to centers of octahedra. Thus there are two types of octahedra, which we denote A and B. This can be directly compared to the pyrochlore, which is the line graph of the bipartite diamond lattice [56]. It will be useful to invoke multiple different unit cells. The primitive 3-site simple cubic unit cell contains

only one octahedron, and is too small to be commensurate with all single-octahedron configurations. Therefore it is convenient to use a conventional 6-site face-centered cubic unit cell containing both an A and a B octahedron. For Monte Carlo simulations, we use a larger conventional 24-site cubic unit cell containing eight octahedra, i.e. the one shown in Fig. 1(a). Details on these unit cell choices are given in Appendix A. For any choice, we assume a lattice consisting of  $L \times L \times L$  unit cells with periodic boundaries. Unless otherwise specified, we work with the 6-site fcc unit cell.

We consider Ising moments  $\mu_i$  located on the sites  $i$  of the octochlore lattice, which we express in terms of  $S_i^z$  via  $\mu_i = (1/2)g_{\parallel} \mu_B S_i^z \hat{z}_i$ , with  $\mu_B$  the Bohr magneton and  $g_{\parallel}$  an ionic Ising  $g$ -factor. In the remainder of this work we treat the  $S_i^z$  as classical Ising variables taking values  $S_i^z = \pm 1$ . The vectors  $\hat{z}_i$  point along the local  $C_{4v}$  easy-axis, and we take the convention to orient these vectors in a bipartite all-in–all-out fashion, pointing from the  $A$  to  $B$  cubic sublattices. Figure 1(a) illustrates the lattice geometry of corner-sharing octahedra, and indicates the first ( $J_1$ ) and second ( $J_2$ ) neighbor interactions. In this work we take the inter-octahedron coupling  $J_{2b}$  to be zero, retaining only the two intra-octahedron couplings  $J_1$  and  $J_{2a}$ , with Hamiltonian

$$H = J_1 \sum_{\langle ij \rangle} S_i^z S_j^z + J_{2a} \sum_{\langle\langle ij \rangle\rangle_a} S_i^z S_j^z. \quad (1)$$

The sign choice of  $J_{2a}$  is such that  $J_{2a} > 0$  prefers ferromagnetic alignment of the moments on opposite corners of an octahedron. Note that, in the 6-site unit cell, the state with all  $S_i^z = 1$  corresponds to the all-out state shown in Fig. 1(b), where antipodal spins are anti-aligned. We parameterize the Hamiltonian with a single angle  $\theta$  and a fixed energy scale  $J > 0$ , as

$$J_1 = J \cos \theta \quad \text{and} \quad J_{2a} = J \sin \theta. \quad (2)$$

We report temperature scales as  $k_B T/J$  with the Boltzmann constant  $k_B$  set to 1.

### A. Irreducible Multipole Moments

Since the  $J_1$  and  $J_{2a}$  interactions are internal to a single octahedron, the Hamiltonian can be expressed as a sum of contributions from each octahedron. Under the action of the octahedral point symmetry group  $O_h$ , a configuration of the six Ising moments on a single tetrahedron can be decomposed into a sum of multipole contributions. The six operators  $S_i^z$  collectively transform in a 6-dimensional representation, which decomposes into irreducible components  $A_{1u} \oplus T_{1g} \oplus E_u$ , corresponding to the monopole, dipole, and diagonal quadrupole

moments, respectively (Appendix B)

$$\begin{aligned} \text{Monopole } (A_{1u}): \quad \phi_o &= \frac{(-1)^o}{\sqrt{6}} \sum_{i \in o} S_i^z, \\ \text{Dipole } (T_{1g}): \quad D_o^\alpha &= \frac{(-1)^o}{\sqrt{2}} \sum_{i \in o} S_i^z \hat{z}_i^\alpha, \\ \text{Quadrupole } (E_u): \quad Q_o^{\alpha\beta} &= \frac{(-1)^o}{\sqrt{2}} \sum_{i \in o} S_i^z \left( \hat{z}_i^\alpha \hat{z}_i^\beta - \frac{1}{3} \delta^{\alpha\beta} \right). \end{aligned} \quad (3)$$

Here,  $o$  labels octahedra and  $\delta$  is the Kronecker delta. The sign  $(-1)^o = +1$  for the  $A$  and  $-1$  for the  $B$  octahedra, corresponding to whether the center of the octahedron labeled  $o$  lies on the  $A$  or  $B$  cubic sublattice. The quadrupole tensor  $Q_o$  is diagonal and trace-free, thus containing only two degrees of freedom corresponding to the two-dimensional  $E_u$  irrep. The chosen normalizations in Eq. (3) ensure that

$$(\phi_o)^2 + |\mathbf{D}_o|^2 + \text{Tr}[Q_o^2] = \sum_{i \in o} (S_i^z)^2. \quad (4)$$

Since the Hamiltonian is bilinear in the  $S_i^z$  and transforms trivially under the symmetry, it can be decomposed on each octahedron into a sum of quadratic invariants (Appendix B)

$$H = \frac{1}{2} \sum_{\text{oct. } o} \left( J_{A_{1u}} |\phi_o|^2 + J_{T_{1g}} |\mathbf{D}_o|^2 + J_{E_u} \text{Tr}[Q_o^2] \right), \quad (5)$$

where the energy of each multipole given by

$$J_{A_{1u}} = 4J_1 + J_{2a}, \quad J_{T_{1g}} = -J_{2a}, \quad J_{E_u} = -2J_1 + J_{2a}. \quad (6)$$

The dependence of energies upon the parameter  $\theta$  in Eq. (2) is shown in Fig. 1(e). The multipole with the lowest energy determines the type of ground state order on each octahedron, dividing the phase diagram broadly into three regions. However, the Ising spin length constraint  $|S_i^z| = 1$  forbids a state with both  $\phi_o = 0$  and  $\mathbf{D}_o = \mathbf{0}$ , i.e. a purely quadrupolar configuration, leading to additional frustration in the  $E_u$  sector that we discuss next.

### B. Fragmentation of the $E_u$ Irrep

Because the Hamiltonian Eq. (5) is quadratic in each multipole moment, the single-octahedron ground state will maximize the lowest-energy multipole and minimize the other two, preferably to zero. This is readily achieved for the monopole moment  $A_{1u}$  irrep—the 6-out configuration shown in Fig. 1(b) has zero dipole and quadrupole moments, and is purely monopolar. The same holds for the dipole moment  $T_{1g}$  irrep—the 3-in-3-out configuration shown in Fig. 1(c) has zero monopole and quadrupole moment, and is purely dipolar. However, this is not the case for the  $E_u$  quadrupole moment irrep: of the  $2^6$  configurations of six Ising spins with  $|S_i^z| = 1$  on a single octahedron, none have *both* zero monopole and dipole moment. (For a complete decomposition of the  $2^6$  states see Appendix B.) Only by violating the spin length con-

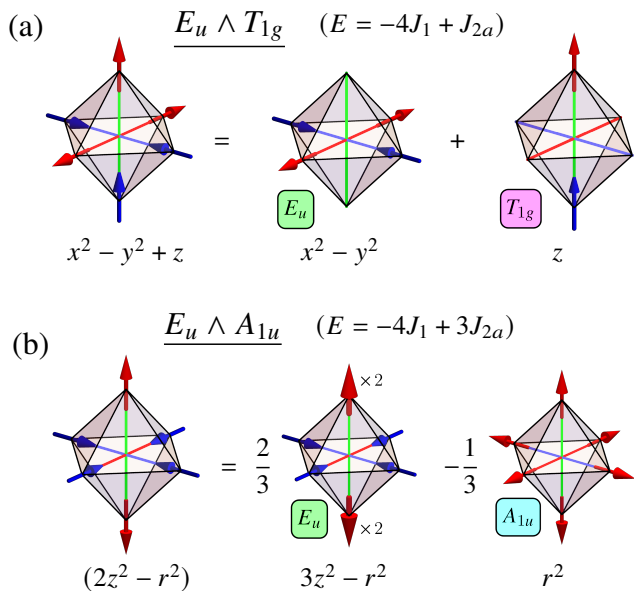


FIG. 2. **Fragmentation of the  $E_u$  irrep.** There are no spin configurations with fixed-length Ising moments,  $S_i^z \in \pm 1$  on all sites, which are purely quadrupolar. Instead, there are two symmetry classes of Ising configurations which mix  $E_u$  with one of the other two irreps. An example of each is given on the left side of (a) and (b). On the right, we decompose each as a linear combination of irreducible monopole ( $A_{1u}$ ), dipole ( $T_{1g}$ ), and quadrupole ( $E_u$ ) configurations with *variable* spin lengths  $S_i^z \in \{0, \pm 1, \pm 2\}$ , where  $S_i^z = 0$  corresponds to the absence of a spin. Beneath each configuration, we have written a polynomial with the corresponding symmetry, where  $r^2 = x^2 + y^2 + z^2$ .

straint can we construct pure- $E_u$  quadrupolar configurations, such as the one shown in Fig. 1(d) with the two apical spins taking the unphysical value  $S_i^z = 2$ , indicated by “ $\times 2$ ”. This configuration is “four-in–four-out”, so it has zero monopole moment, and also has zero net dipole moment along each of the three axes. Thus it is purely quadrupolar, but at the cost of violating the spin length constraint. We refer to this obstruction to a pure-quadrupolar ground state as “frustration of the  $E_u$  irrep” by the spin length constraint.<sup>1</sup>

At the single-octahedron level, the consequences of this irrep frustration is that the configurations which maximize the quadrupole moment are “fragmented” [43, 66, 68], meaning that they mix  $E_u$  with one of the other two irreps. This is illustrated in Fig. 2. There are two symmetry-inequivalent classes of maximal- $E_u$  configurations, mixing  $E_u$  with either  $T_{1g}$  or  $A_{1u}$ . One member of each class is shown on the left hand side of the equations in Fig. 2(a,b). We refer to these configurations as  $E_u \wedge T_{1g}$  and  $E_u \wedge A_{1u}$ . On the right hand

side, we have decomposed each as a linear combination of an  $E_u$  component and either a  $T_{1g}$  or an  $A_{1u}$  component. Beneath each we provide a polynomial which reflects the symmetry of this irrep—a monopole transforms like  $r^2$ , dipoles transform like  $x$ ,  $y$ , and  $z$ , and the two-component  $E_u$  quadrupole transforms like  $3z^2 - r^2$  and  $x^2 - y^2$ . In the  $E_u$  sector of the phase diagram, i.e. the parameter region where  $J_{E_u} < J_{A_{1u}}, J_{T_{1g}}$ , one of these two fragmented configurations will have lower energy, with Fig. 2(a) having lower energy when  $J_{2a} > 0$  and Fig. 2(b) having lower energy when  $J_{2a} < 0$ . This therefore subdivides the  $E_u$  sector into two distinct ground state phases.

### III. PHASE DIAGRAM

In this section we summarize the contents of the phase diagram of the Hamiltonian Eq. (1), while the remainder of the paper focuses in detail on specific portions of it. Figure 1(f) shows the phase diagram parameterized by an angle  $\theta$ , defined in Eq. (2). The radial axis is temperature  $T/J$ , with  $T = 0$  at the outer edge increasing towards infinite temperature at the center of the disk. The outer edge of the disk is colored according to the single-octahedron ground state irrep(s): blue for  $A_{1u}$ , Fig. 1(b); magenta for  $T_{1g}$ , Fig. 1(c); hatched green-blue for  $E_u \wedge A_{1u}$ , Fig. 2(a); and hatched green-magenta for  $E_u \wedge T_{1g}$ , Fig. 2(b). The phase diagram is correspondingly divided into four quadrants by solid lines, each with a different set of ground state spin configurations. We have performed classical Monte Carlo simulations to determine finite-temperature phase boundaries, indicated by black dots (details of the Monte Carlo simulations are provided in Appendix F).

#### A. Degeneracies and Flat Bands

Table I summarizes the four phases and phase boundaries, discussed in more detail below, including their zero-temperature ground state degeneracies. Most notably, only the  $A_{1u}$  phase exhibits ordinary symmetry breaking long-range order; all other parts of the phase diagram exhibit either extensive or subextensive ground state degeneracies.<sup>2</sup> Extensive ground states are characteristic of spin liquids, which are known to occur at multi-critical points [22, 23]. Subextensive ground state degeneracies are intermediate between spin liquids and long-range order, and are comparatively less studied.

In addition, we provide the zero-energy locus of the band structure of the Hamiltonian. A quadratic spin Hamiltonian can be written as  $H = E_0 + \sum_{ij} \mathcal{J}_{ij} S_i^z S_j^z$ , where  $E_0$  is the ground state energy and  $\mathcal{J}$  is the interaction matrix encoding two-spin interactions, shifted to have minimum eigenvalue

<sup>1</sup> It is worth noting that this frustration is of the same type as occurs in the 2D nearest-neighbor kagome Ising model, where the frustrated cluster is a triangle of three spins, and the irreps are a 1D monopole and 2D dipole moment. The putative spin ice phase of this model should maximize the dipole moment and minimize the monopole moment, but this is not possible due to the spin length constraint. In that case the system is forced to remain trivially paramagnetic at all temperatures [67].

<sup>2</sup> For simplicity, we refer to the low-temperature regimes as “phases”, even though adding additional further-neighbor interactions like  $J_{2b}$  will lead to some selection of an order-unity number of ground states out of these massive ground state manifolds. From the perspective of an extended phase diagram including such interactions, the parameter regions with (sub)extensive ground state degeneracies will be phase boundaries or multicritical loci.

Phase	Description	$\log_2(\text{GSD})$	Order Type	Zero-Energy Locus
$A_{1u}$	All-In–All-Out	1	SSB [ $\mathbb{Z}_2$ ]	0D: Zone Corner
$T_{1g}$	Frustrated Chains	$\propto L^2$	Unknown	2D: $\{hk0\}$ Planes
$E_u \wedge T_{1g}$	Fragmented Spin Ice	$\propto L^3$	Spin Liquid [U(1) Coulomb]	1D: Zone Edges <sup>†</sup>
$E_u \wedge A_{1u}$	Spin Nematic [Uniaxial / Biaxial]	$\propto L^2$	SSB [ $O_h$ ] / Dim. Reduction	1D: Zone Edges <sup>†</sup>
Boundary	Description	$\log_2(\text{GSD})$	Order Type	Zero-Energy Locus
$[E_u \wedge T_{1g}] \oplus T_{1g}$	Spin Ice	$\propto L^3$	Spin Liquid [U(1) Coulomb]	3D: FB $\times 2 + (000)$
$[A_{1u} \oplus T_{1g}]$	X-cube	$\propto L^3$	Spin Liquid [U(1) Fracton]	3D: FB $\times 1 + \{00\ell\}$
$[E_u \wedge T_{1g}] \oplus [E_u \wedge A_{1u}]$	Paramagnet	$\propto L^3$	Paramagnet [ $J_{2a} = 0$ ]	1D: Zone Edges <sup>†</sup>
$[E_u \wedge A_{1u}] \oplus A_{1u}$	Decoupled AFM Chains	$\propto L^2$	1D Critical [ $J_1 = 0$ ]	2D: $\{hk0\}$ Planes

TABLE I. **Summary of the phases and phase boundaries that appear in the phase diagram of Fig. 1(f).** Quadrants are labeled by the relevant ground state irreps, with the two fragmented  $E_u$  ground states indicated using the notation in Fig. 2. Boundaries are labeled by the degenerate combination of irreps. We provide a description of each, the system-size scaling of the ground state degeneracy (GSD), and order type of the low-temperature phase: a phase with spontaneous symmetry breaking (SSB), a classical spin liquid, or otherwise. The last column lists the zero-energy locus of the interaction matrix band structure. Cases with flat bands (FB) provide the number of bands and the locus where dispersive bands touch the flat bands. Cases marked <sup>†</sup> are fragmented, so the flat locus is not directly reflective of the ground state degeneracies.

zero. The interaction matrix can be diagonalized by Fourier transform, its eigenvalues forming a set of bands  $\mathcal{J}_n(\mathbf{q})$  where  $\mathbf{q}$  are reciprocal space wavevectors and  $n$  indexes the bands, equal to the number of degrees of freedom in the primitive unit cell. If the spins are treated as “soft” degrees of freedom, i.e. in a self-consistent Gaussian approximation [69] where the  $S_i^z$  vary continuously with an average spin length constraint (Appendix D), then the ground state order is determined by the eigenvectors of  $\mathcal{J}$  with zero eigenvalue. Classical spin liquids can then be identified with a set of zero-energy flat bands in the spectrum of  $\mathcal{J}$ , signaling an extensive ground state manifold [17, 18, 70]. Indeed the  $A_{1u}$  phase exhibits a single band minimum, exhibiting an essentially unique ground state, while all other points in the phase diagram exhibit either an extensive or sub-extensively degenerate zero-energy locus. Sub-extensively degenerate loci are intermediate between completely flat bands and discrete minima, and signal potential exotic physics intermediate between spin liquids and long-range order.<sup>3</sup>

In the rest of this section we summarize the variety of low-temperature behaviors observed in the entire phase diagram, before diving into detailed investigations in the remainder of the paper. For ease of presentation, we start with the four fine-tuned phase boundaries, marked by colored diamonds in Fig. 1(f). We then turn to the four phases, indicated by colored arcs on the outer edge of the disk in Fig. 1(f). In this section, we denote the Hamiltonian relative to the ground state energy as

$$\tilde{H}(J_1, J_{2a}) \equiv H(J_1, J_{2a}) - E_0(J_1, J_{2a}), \quad (7)$$

<sup>3</sup> Perhaps the best-studied example is the antiferromagnetic nearest-neighbor Ising model on the FCC lattice, whose interaction matrix exhibits flat  $\{10\ell\}$  lines along the zone boundary and has a subextensive ground state degeneracy [71, 72]. It undergoes a first order transition at finite temperature which selects ground states consisting of AFM-ordered planes [73, 74] driven by an order-by-disorder mechanism [72, 75].

where  $H$  is the Hamiltonian, Eq. (1), and  $E_0$  is the ground state energy, each a function of the interaction parameters  $J_1$  and  $J_{2a}$ .

## B. Phase Boundaries

$\diamond (E_u \wedge T_{1g}) \oplus T_{1g}$  — Denoted in the phase diagram by a blue diamond, at this point, the Hamiltonian relative to the ground state energy reduces to

$$\tilde{H}_{\text{spin ice}} \propto \sum_{\mathbf{o}} |\phi_{\mathbf{o}}|^2. \quad (8)$$

The single-octahedron ground states satisfy a zero-divergence 3-in–3-out “ice rule” constraint, and the system realizes a U(1) Coulomb phase [56]<sup>4</sup>, or equivalently a loop gas [59, 76] or condensate [65]. Minimal excitations are point particles carrying  $A_{1u}$  “monopole moments” [15], as indicated by the energy cost of creating  $\phi_{\mathbf{o}}$  monopoles in  $\tilde{H}_{\text{spin ice}}$  of Eq. (8). The interaction matrix exhibits two zero-energy flat bands, with one quadratically dispersing band that touches the flat bands at the zone center. This band structure corresponds to a long-wavelength free-energy of the form  $\int (\nabla \cdot \mathbf{D})^2$ , where  $\mathbf{D}$  is the coarse-grained dipole moment [56, 77]. Microscopically, the flat bands give rise to zero-energy collective loop flips of head-to-tail spins [43, 63, 76].

$\diamond (E_u \wedge A_{1u}) \oplus A_{1u}$  — Denoted in the phase diagram by a magenta diamond, at this point the Hamiltonian relative to the ground state energy reduces to

$$\tilde{H}_{\text{AFM chains}} \propto \sum_{\mathbf{o}} |\mathbf{D}_{\mathbf{o}}|^2 \quad (9)$$

<sup>4</sup> The fact that this is a U(1) spin liquid refers to the fact that in the ground state manifold, satisfying a zero-divergence constraint, the conserved flux through closed surfaces is integer-valued, as in a U(1) gauge theory [37].

This point has  $J_1 = 0$ , and the Hamiltonian splits into decoupled 1D antiferromagnetic (AFM) chains, illustrated in Fig. 1(a) by colored lines along each of the Cartesian direction. Each chain has two Néel ground states, but they do not order at any finite temperature. Excitations are deconfined antiferro-spinons, which can move freely along a chain by flipping spins at zero energy cost. It is clear from Eq. (9) that the excitations are charged in the  $T_{1g}$  irrep, meaning that these quasiparticles carry a dipole moment. The direction of this local dipole moment switches as the quasiparticle hops on the Néel background, but the staggered dipole moment  $\mathbf{D}_o$  is conserved (staggered by the alternating sign  $(-1)^o$  in Eq. (3)).

◊  $\mathbf{A}_{1u} \oplus \mathbf{T}_{1g}$  — Denoted in the phase diagram by a green diamond, this point is the focus of Section V. At this point, the Hamiltonian relative to the ground state energy reduces to

$$\tilde{H}_{X\text{-cube}} \propto \sum_o \text{Tr}[Q_o^2] \quad (10)$$

We will demonstrate that it realizes a previously unreported *fracton CSL*. We identify it as a classical U(1) version of the X-cube topological order [62, 78]. Using a tailored cluster Monte Carlo algorithm, we demonstrate that it is stable down to zero temperature. Unlike the spin ice CSL, whose ground state manifold is a loop gas or string-net condensate, the X-cube CSL can be described instead as a cage-net condensate [64], where the minimal zero-energy moves involve not loops but closed cage-like structures. The excitations in this phase carry an  $E_u$  quadrupole moment, and we will show that they are sub-dimensional “lineon” quasiparticles. In particular, particles carrying  $(3z^2 - r^2)$  quadrupole charge are restricted to move along the  $z$  direction, and similarly for the  $x$  and  $y$  directions.

◊  $(E_u \wedge T_{1g}) \oplus (E_u \wedge A_{1u})$  — Denoted in the phase diagram by a white diamond, this  $J_{2a} = 0$  point is the nearest-neighbor Ising AFM on the octochlore lattice [79, 80]. At this point, the two fragmented  $E_u$  configurations in Fig. 2 become degenerate. There is no finite-temperature phase transition, so the ground state is paramagnetic [80]. However, notice that a  $E_u \wedge T_{1g}$  (Fig. 2(a)) configuration can be converted into an  $E_u \wedge A_{1u}$  (Fig. 2(b)) configuration and vice-versa by flipping a single spin. It follows that in a ground state consisting of a mixture of these two octahedral configurations, there will exist a finite density of single spins that can freely flip without changing the energy at zero temperature. This implies that the system remains a trivial paramagnet with only short-range correlations to zero temperature, and does not realize a CSL.

### C. Phases

◦  $\mathbf{A}_{1u}$  — Denoted in the phase diagram by a cyan arc, in this phase the single-octahedron ground states are either 6-in or 6-out, such as shown in Fig. 1(b), and the global ground states are the two “all-in/all-out” (AIAO) ground states. This is the only phase portion of the phase diagram exhibiting an order-unity ground state degeneracy and magnetic long-range order. The low temperature phase breaks the global  $\mathbb{Z}_2$  time-reversal and inversion symmetries (but preserves their product). The

symmetry-breaking order parameter is the scalar

$$\phi = \frac{1}{N_o} \sum_o \frac{1}{\sqrt{6}} (-1)^o \phi_o, \quad (11)$$

where  $N_o$  is the number of octahedra in the lattice, normalized so that  $|\phi|^2 \leq 1$ . This phase sits opposite the spin ice CSL in the phase diagram. In particular, it contains the point where the Hamiltonian is given by  $-\tilde{H}_{\text{spin ice}}$  [cf. Eq. (8)], marked in the phase diagram with a cyan disk. Therefore, its ground state can be said to maximize the divergence of the dipole configuration at every octahedron. One may view each ground state as a maximally packed crystal of  $\pm 3$ -charged monopole quasiparticles [66] on the two cubic sublattices in an NaCl-type arrangement. Indeed, the scalar order parameter Eq. (11) may be viewed as a measure of the “monopole contrast” between the two sublattices,  $\phi \propto \sum_{o \in A} \phi_o - \sum_{o \in B} \phi_o$ , i.e. the staggered monopole density.

◦  $E_u \wedge T_{1g}$  — Denoted in the phase diagram by a hatched green-magenta arc, in this phase the single-octahedron ground states are the fragmented configurations shown in Fig. 2(a). These are a subset of the 3-in–3-out spin ice configurations. Reference [43] showed that these configurations are sufficient to preserve an extensive ground state manifold, giving a CSL that is a restricted version of spin ice dubbed “fragmented spin ice” (FSI). This is a U(1) Coulomb phase like spin ice, with algebraic correlations and 2-fold pinch points. Excitations include the monopoles of spin ice, but additionally the  $E_u \wedge T_{1g}$  states (Fig. 1(c)), which have zero monopole moment, are also gapped low-energy excitations. The latter can be viewed as an energy cost for particular types of loop configurations in the loop-gas picture of the spin ice ground state manifold; the stability of the spin liquid means that these energetic restrictions on loop configurations are an irrelevant perturbation to the long-wavelength Coulomb description.

◦  $\mathbf{T}_{1g}$  — Denoted in the phase diagram by a magenta arc, this phase is the focus of Section IV. In this phase, the single-octahedron ground states are the configurations shown in Fig. 1(c). This phase sits opposite the decoupled AFM chains point, in particular, it contains the point where the Hamiltonian is given  $-\tilde{H}_{\text{AFM chains}}$  [Eq. (9)], marked in the phase diagram with a magenta disk. Its ground states can therefore be formally described as maximal packings of antiferro-spinons. Naively, one might expect this phase to exhibit long-range magnetic order with macroscopic dipole moment,

$$\mathbf{D} = \frac{1}{N_o} \sum_o \frac{1}{\sqrt{6}} (-1)^o \mathbf{D}_o, \quad (12)$$

where  $N_o$  is the number of octahedra in the lattice, normalized so that  $|\mathbf{D}|^2 \leq 1$ . The situation is not so simple, however. At the special point with  $J_1 = 0$ , the system is decoupled into 1D ferromagnetic (FM) chains, every chain having two ground states, and the minimal excitations are deconfined 1D ferro-spinons. Since the chains polarize independently, the net dipole moment of the system is zero. We find that turning on  $J_1 \neq 0$  does not lift the subextensive ground state degeneracy, and we therefore dub this the frustrated chains phase.

Rather, the chains interact only indirectly via collisions between spinons moving on orthogonal chains. Our Monte Carlo simulations do not find clear signatures of symmetry-breaking order in this phase. Notably, however, the spin ice and X-cube CSL's appear at the endpoints of this phase. We show that their existence and physical properties can be rationalized by viewing them as condensates of 1D ferro-spinon bound states.

◦  $E_u \wedge A_{1u}$  — Denoted in the phase diagram by a hatched green-cyan arc, this phase is the focus of Section VI. In this phase, the single-octahedron ground states are the fragmented configurations shown in Fig. 2(a). This phase sits opposite the fracton CSL, in particular, it contains the point where the Hamiltonian is given by  $-\tilde{H}_{X\text{-cube}}$  [Eq. (10)], marked in the phase diagram with a green disk. Therefore, its ground states can be viewed as a maximal packing of the  $E_u$ -charged lineon quasiparticles. Using Monte Carlo, we identify two finite-temperature transitions upon cooling: the first develops uniaxial nematic order, with symmetry reducing from cubic to tetragonal; the second develops biaxial nematic order, further reducing the symmetry to orthorhombic. These are detected by the global quadrupole tensor order parameter,

$$Q^{\alpha\beta} = \frac{1}{N_o} \sum_o \frac{\sqrt{3}}{4} (-1)^o Q_o^{\alpha\beta}. \quad (13)$$

where  $N_o$  is the number of octahedra in the lattice, normalized so that  $\text{Tr}[Q^2] \leq 1$ . The transition to uniaxial order can be readily described in the Landau symmetry-breaking paradigm, where the system lowers its free energy energetically by turning on the quadrupolar order parameter. However, we demonstrate that the transition to biaxial order is fluctuation-driven: by ordering along a second axis, the system is able to support deconfined antiferro-spinons, which are free to disorder chains along the third axis, maximizing entropy and thereby minimizing the free energy, preventing the selection of a unique ground state out of subextensively many.

This completes our review of the phase diagram Fig. 1(f), summarized in Table I. In the remainder of this paper, we study the three most interesting parts of the phase diagram, exhibiting novel physics. Section IV focuses on the  $T_{1g}$  frustrated chains phase, from which we will develop an intuitive understanding of the origin of the spin ice and fracton CSLs which occur at its endpoints, and their fractionalized excitations. Section V then explores in detail the  $T_{1g} \oplus A_{1u}$  fracton CSL and establishes its basic properties. Finally, aided by a solid understanding of the fracton CSL, Section VI studies the most complex part of the phase diagram, the spin nematic  $E_u \wedge A_{1u}$  phase.

#### IV. $T_{1g}$ FRUSTRATED CHAINS PHASE

In this section, we investigate the  $T_{1g}$  phase, indicated by the magenta arc at the top of the phase diagram, Fig. 1(f). We dub this the frustrated chains phase, as it has a subextensively degenerate ground state manifold on polarized chains. We expose the origin of interchain interactions, via spinon collisions, and the fate of the equilibrium state at low temperatures. In the process, we uncover the mechanism by which the spin ice and

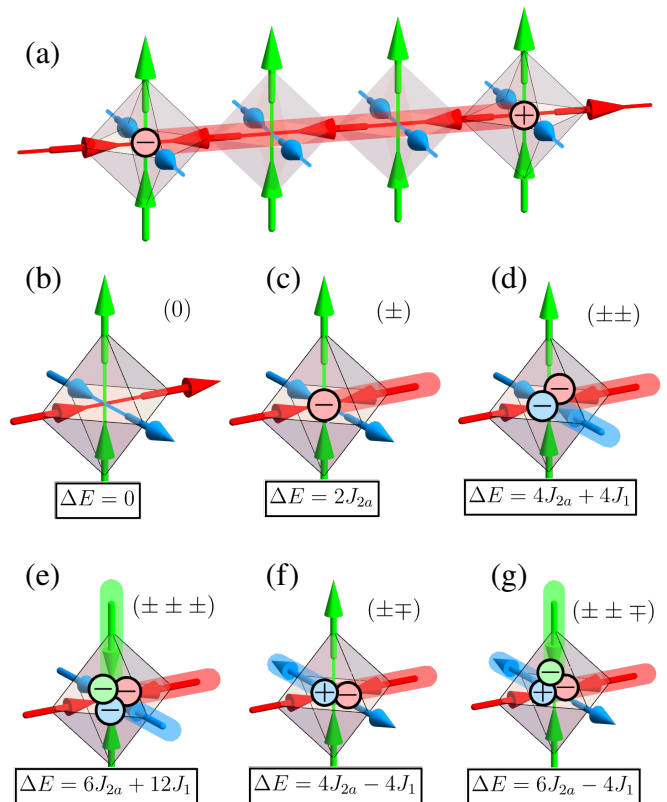


FIG. 3. **1D spinon interactions in the  $T_{1g}$  phase.** (a) When  $J_1 = 0$ , the system decouples into 1D Ising chains. For  $J_{2a} > 0$ , each chain is ferromagnetic, and the fundamental excitations are positive and negative charged spinons created from a ground state by flipping a straight open string (chain segment) of head-to-tail spins, denoted by the red tube. (b) For small  $|J_1|$ , the energy of the polarized chain states does not change, and the system retains a subextensive ground state degeneracy. (c) The single-spinon energy gap is  $2J_{2a}$ , independent of  $J_1$ . (d-g) A finite positive (negative)  $J_1$  introduces attraction (repulsion) between spinons of opposite charge.

X-cube spin liquids arise at the ends of this phase, via spinon bound state condensation.

##### A. Chain Interactions via 1D Spinon Collisions

In the center of this phase is a special point where  $J_1 = 0$ , marked with a magenta disk. At this point, the Hamiltonian decouples into 1D ferromagnetic Ising chains running along each of the cubic [001] directions. Each chain has two fully-polarized ground states, so the zero-temperature entropy is proportional to the number of chains,  $\propto L^2$ , where  $L$  is the linear size of the system. These 1D chains do not order at any finite temperature because the domain wall excitations—spinons—are deconfined. By the standard Peierls argument, their configurational entropy massively outweighs their energetic cost. The decoupled chains are instead critical, with a diverging correlation length as  $T \rightarrow 0$ .

Now consider coupling the chains with a non-zero  $J_1$ . On each octahedron, the ground states are the six pure- $T_{1g}$  configu-

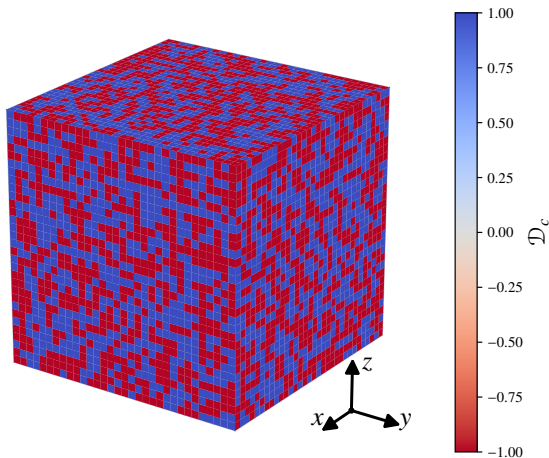


FIG. 4. **Randomly polarized chains in the  $T_{1g}$  phase.** A snapshot of the value the chain ferromagnetic order parameters  $\mathcal{D}_c$ , Eq. (14), where each chain is associated with a point on the surface of a cube. This snapshot is from a system with 32 spins per chain that has been slowly annealed from high temperature. In our simulations we always find that the chains adopt an essentially random polarization across the entire  $T_{1g}$  frustrated chains phase.

rations, such as the one shown in Fig. 1(c), for which antipodal spins are ferromagnetically aligned. These configurations are all symmetry-equivalent under the action of the point group, so a non-zero  $J_1$  interaction cannot create any energetic preference among them. Therefore, any configuration of polarized chains remains a ground state when  $J_1 \neq 0$ , and the system retains subextensive ground state degeneracy throughout the entire  $T_{1g}$  phase—the ferromagnetic chains are frustrated.

One-dimensional Ising chains are the prototypical example of fractionalization: single spin flips deconfine into pairs of spinons (domain walls) at the ends of open strings of head-to-tail spins, as depicted in Fig. 3(a). Starting with  $J_1 = 0$ , each spinon costs energy  $2J_{2a}$ . Turning on  $J_1 \neq 0$  does not shift the ground state or single-spinon energies; rather, it induces interactions between spinons in different chains when they reside on the same octahedron. This is illustrated in Fig. 3(b-g), where spinons on the three orthogonal chains through an octahedron are colored red, blue, and green. Thus, different chains only couple to each other when a spinon moving along one chain collides with a spinon moving along another, orthogonal chain.

## B. Low-Temperature Behavior

At low temperatures, the spinon density is exponentially suppressed, such that collisions are extremely rare, and the system retains quasi-1D decoupled chain behavior. At higher temperatures, the thermal proliferation of spinons allows the chains to interact via spinon collisions, and eventually the system enters the 3D paramagnetic phase. It is not immediately clear whether a phase transition must occur between

these two limits, since a 3D paramagnet and 1D chains are both disordered at finite temperature. Thus, there are two possibilities: either the system exhibits a smooth crossover to a low-temperature limit of disordered, deconfined, and effectively non-interacting chains, or it undergoes a sharp phase transition at finite temperature.

Numerically resolving which scenario is realized is difficult, particularly in the vicinity of the decoupled  $J_1 = 0$  limit, due to the exponentially growing correlation length of the 1D chains. Specifically, the density of gapped spinons on a chain at low temperatures scales as  $\exp(-2J_{2a}/T)$ ; Once the density of spinons in the system is less than order one per site all chains will be polarized, which occurs at a temperature scale of  $T_*(L) \sim J_{2a}/\log(L)$ . This means that exponentially large system sizes are required to explore the low-temperature regime near the decoupled-chain limit.

If a transition does occur, it is not clear what order parameter can capture it. The simplest possibility is the net dipole moment, Eq. (12). However, in our Monte Carlo simulations, we always find apparently random patterns of chain polarizations at low temperature. Using the 3-site unit cell (Appendix A), define a ferromagnetic order parameter for each chain  $c$

$$\mathcal{D}_c = \frac{1}{L} \sum_{i \in c} S_i^z \in [-1, 1] \quad (3\text{-site unit cell}), \quad (14)$$

which measures the net polarization of the chain. We show in Fig. 4 a snapshot obtained from annealing an  $L = 32$  system to low temperature, where we have plotted the values of  $\mathcal{D}_c$  for each chain represented as a point on the surface of a cube. The system never develops an appreciable net dipole moment as the random chain polarizations tend to cancel each other.

Reference [43] reports a sharp low-temperature specific heat anomaly when weakly perturbing away from the spin ice point into the  $T_{1g}$  phase. We were able to reproduce this, but the anomaly is only detectable very close to the  $J_{2a} = J_1$  spin ice point but is undetectable deeper in the  $T_{1g}$  phase away from the spin ice point. This anomaly could be a transition or a very rapid crossover which broadens away from the spin ice point, but we have not determined which is the case. At temperatures below the anomaly, we still find that the chains polarize in an uncorrelated fashion.

It is worth pointing out that an analogous situation occurs in the  $J_1$ - $J_{2a}$  checkerboard lattice Ising model, where  $J_{2a} > J_1$  selects a subextensive set of polarized-chain ground states [81]. As far as we are aware, the nature of the finite-temperature transition in that model, if it exists, has also not been established, though the corresponding ground state manifold in the 6-vertex model is disordered [82].<sup>5</sup> Without a concrete signature of symmetry breaking and an order parameter to detect it, we cannot resolve the question either way, and we leave this problem for future study. Our finding of randomly polar-

<sup>5</sup> In Baxter's phase diagram for the 6-vertex model, Fig. 8.5 of Ref. [82], the polarized chain ground states are reached on the line  $a/c = b/c = x > 1$  in the limit  $x \rightarrow \infty$ , and this line always lies in the disordered region labeled III.

ized chains and a lack of a clear specific heat anomaly in the majority of the phase is consistent with a disordered scenario.

### C. Spin Liquids from Condensation of Spinon Bound States

Setting aside the precise nature of the low-temperature fate of the frustrated chains regime, examining more closely the behavior of the multi-spinon interactions in Fig. 3 yields remarkable insight into what happens at the *boundaries* of the  $T_{1g}$  phase, where the  $T_{1g}$  irrep becomes degenerate with either the  $A_{1u}$  or  $E_u$  irreps and the system passes from this frustrated chains regime to two different CSLs.

Figure 5(a) shows the change in the multi-spinon energies as  $J_1$  is varied. When  $J_1 > 0$ , the energy of the spinon/anti-spinon pair, shown in Fig. 3(f), decreases until these bound states *condense* (become degenerate with the spinon vacuum) when  $J_1/J_{2a} \rightarrow 1$ . That is, Fig. 3(f) has the same energy as Fig. 3(b). Spinon/anti-spinon condensation implies that the three colors of spinons, corresponding to the three chain directions, become *indistinguishable*, which is illustrated in Fig. 5(b): a green spinon moving along its chain (by flipping spins) can freely transmute to a red spinon by nucleating an anti-green/red pair from the vacuum, allowing it “turn a corner” and move along a red chain; it may then further transmute to a blue spinon to move along a blue chain. Thus, the system has only a single type of spinon, which is a fully mobile 3D quasiparticle. These are precisely the monopoles of the spin ice CSL.

Viewing spinon trajectories as strings of flipped spins, as in Fig. 3(a), this pattern of spinon condensation allows strings from different chains to be joined end-to-end without paying any energy at the “corner” where they meet. Hence, they can form arbitrary closed loops in 3D, resulting in a classical string-net condensate [65]—a 3D Coulomb CSL [56]. From the perspective of the loop gas picture [76] of the spin ice CSL, the spinon/anti-spinon pair energy may be viewed as an energetic cost for “bending” loops. Furthermore, since spinons are excitations on top of a pure- $T_{1g}$  ground state, they carry both an  $E_u$  and  $A_{1u}$  moment; condensing the spinon/anti-spinon pairs makes the  $E_u$  quadrupole component “invisible”, so the resulting spin ice spinons carry only an  $A_{1u}$  monopole moment, as is clear from the Hamiltonian Eq. (8).

These arguments illustrate how spin ice arises from coupling intersecting ferromagnetic chains by condensation of spinon bound states. One may then wonder what type of CSL might be produced by a different pattern of spinon condensation at the opposite end of the frustrated chains phase, with  $J_1 < 0$ . As  $J_1/J_{2a} \rightarrow -1/2$ , the *triple spinon* ( $\pm \pm \pm$ ) bound states, shown in Fig. 3(e), condense into the vacuum. This yields a new CSL with completely distinct physics to spin ice, which we explore in detail in the next section.

### V. $T_{1g} \oplus A_{1u}$ CAGE-NET FRACTON SPIN LIQUID

In this section, we provide a detailed account of the properties of the spin liquid that arises at the point  $J_1/J_{2a} = -1/2$ .

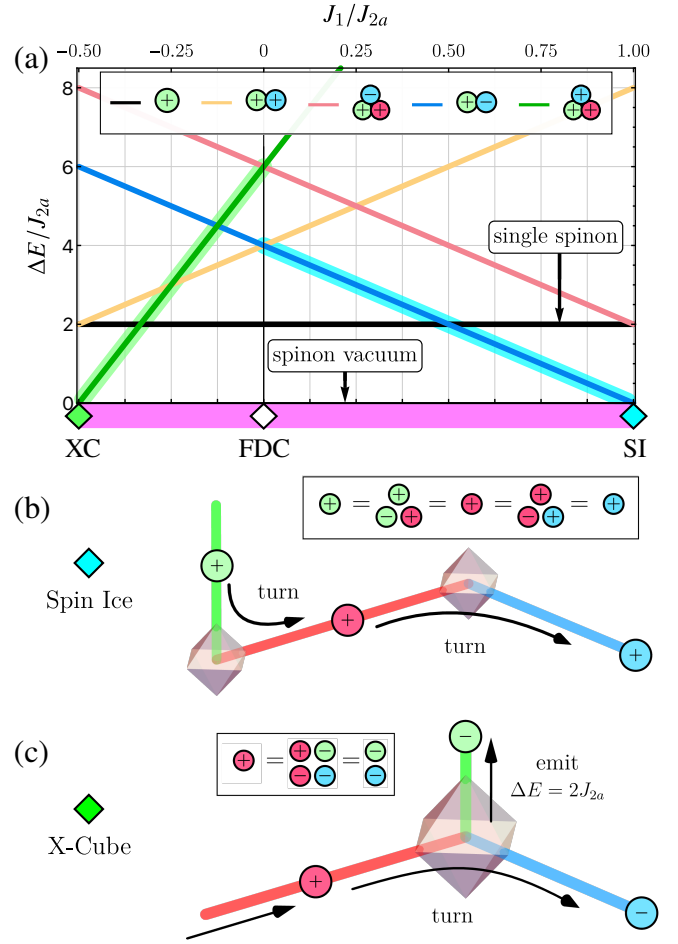


FIG. 5. **Spin liquids from 1D spinon condensation.** (a) Variation of multi-spinon energies with  $J_1/J_{2a}$ . Pairs of oppositely charged spinons [Fig. 3(f)] condense at the spin ice point  $J_1/J_{2a} = 1$ , while triple-charges bound states [Fig. 3(e)] condense at the X-cube point  $J_1/J_{2a} = -1/2$ , giving rise to two different CSLs. (b) At the spin ice point, a single spinon can turn a corner onto an orthogonal chain without costing any energy; there is no distinction between the colors of spinons, they are free to move in 3D. (c) At the X-cube point, a spinon can *only* turn a corner by changing its sign and emitting a spinon along the third orthogonal chain, which costs an energy  $2J_{2a}$ . Thus, individual spinons are confined to move along 1D lines—they are lineons.

As we will see, the condensation of the triple spinon bound states gives rise to a *fracton* CSL. Tracking the evolution of energies in Fig. 5(a), it is clear that the minimal excitation of this CSL is a single spinon, which is degenerate with a pair of same-charge spinons. As shown in the inset of Fig. 5(c), condensation of triple spinon bound states implies that a red spinon is equivalent to a blue-green bound state of anti-spinons. A single spinon can only “turn a corner” by splitting this bound state apart, effectively emitting a third spinon along the orthogonal chain as depicted in Fig. 5(c). This maneuver costs  $2J_{2a}$  energy, constraining the propagation of the minimal excitations of this CSL to straight lines along their chain. In other words, these excitations are “lineons”, quasiparticles with sub-dimensional mobility along a line [34]. Such sub-dimensional

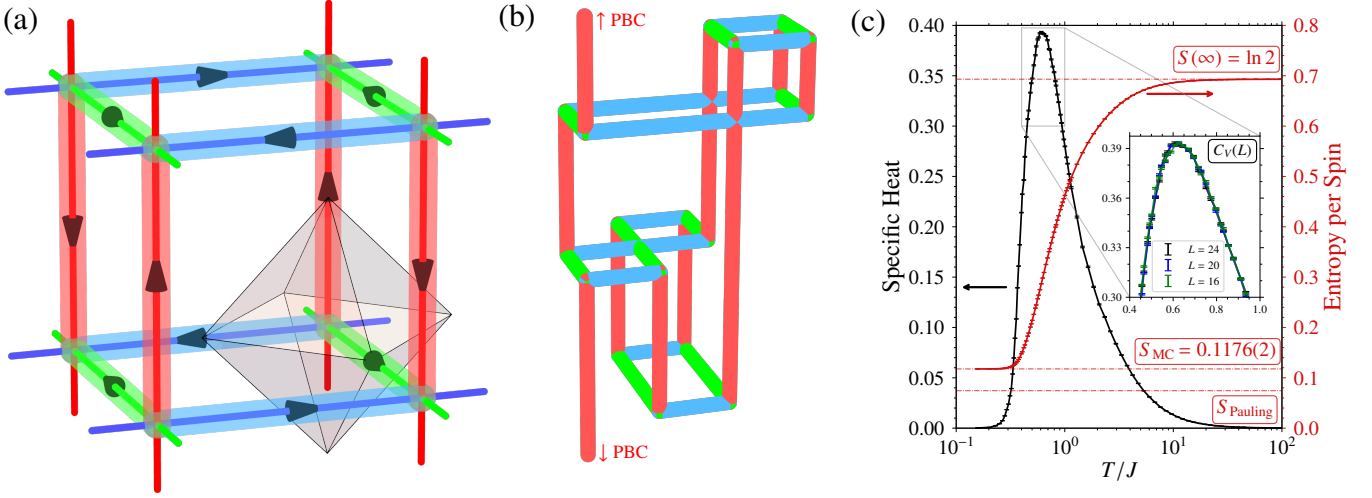


FIG. 6. **Cage-net fracton spin liquid.** (a) Ising spins (black arrowheads) may be viewed as lying along edges of the parent cubic lattice (thin colored lines). The minimal local zero-energy collective spin flip is a closed cage of twelve spins on the edges of a cube in the arrangement shown. (b) An illustration of a larger “cage-net” flippable motif, which may close around the periodic boundaries (PBC). At zero temperature, such collective flips “tunnel” the system between degenerate vacua. (c) Specific heat (left axis indicated by black left-pointing arrow) and entropy per spin (right vertical axis, indicated by right-pointing red arrow) of the fracton spin liquid obtained from cluster Monte Carlo simulation with linear dimension  $L = 24$ . The inset shows a lack of system-size scaling of the specific heat maximum with respect to system size for  $L = 16, 20, 24$ , indicating a smooth crossover and no transition. Simulations are performed with the 24-site unit cell (Appendix A), simulation details are provided in Appendix F.

mobility is the hallmark of fractonic phases of matter [32, 83].<sup>6</sup> The  $(\pm\pm\pm)$  condensation pattern implies that lineons can only be created and annihilated in red-blue-green trios.

### A. Cage-Net Tunneling Between Ground States

A classical spin liquid is characterized by a local constraint. According to Eq. (10), the local constraint is that each octahedron has zero  $E_u$  quadrupole moment,  $Q_o = 0$ . Equivalently, the CSL is characterized by its ground state (vacuum) manifold and the zero-energy collective spin flips, which tunnel the system between different vacua. These tunneling moves should be viewed as processes by which charges are locally nucleated from the vacuum, moved around, and recombined to create a vacuum configuration differing from the original by a local move. The simplest example is the spin ice CSL, which can be viewed as a condensate of spinon/anti-spinon pairs. Nucleating such a pair from the vacuum, it can be split apart at energy cost  $2 \times 2J_{2a}$ , then one of the spinons can be propagated around a closed path (by flipping spins), and the pair re-annihilated to return to a vacuum configuration. The resulting collective spin flip is often called a loop move, and forms the basis for efficient numerical Monte Carlo simulation of spin ice physics [63, 76].

Applying this logic to the triple-spinon-condensed CSL, we begin by nucleating a spinon trio at one site and splitting it apart by hopping each of the three spinons one tetrahedron along  $+\hat{x}$ ,  $+\hat{y}$ , and  $+\hat{z}$ . Each of these can then be split into a pair of anti-spinons as in Fig. 5(c). For the spinon located at  $+\hat{x}$ , we move its anti-spinons  $\hat{y}$  and  $\hat{z}$ , and similarly for the other two spinons. This results in an anti-spinon pair, equivalent to a single spinon each, located at the three octahedra at  $\hat{x} + \hat{y}$ ,  $\hat{x} + \hat{z}$ , and  $\hat{y} + \hat{z}$ . These three spinons can then be moved to the octahedron at  $\hat{x} + \hat{y} + \hat{z}$  and annihilate to return to the vacuum. The minimal zero-energy spin flip is therefore the flip of a cube as shown in Fig. 6(a), where arrows indicate the relative directions the spins must point for this cluster to be flippable at zero energy cost. Note that as a process of flipping single spins, this requires passing through intermediate states with at least four excitations, with energy  $4 \times 2J_{2a}$ .

This cube move is the smallest possible flippable cluster, involving twelve spins. Larger clusters can be formed by such spinon proliferation and recombination processes, and we refer to these in general as “cage moves”, by analogy with the “loop moves” of spin ice [63, 76]. In particular, one can combine many copies of the minimal cube to form large contractible flippable cages. General cages can be built from straight oriented segments representing lineon trajectories, which are glued together at corners where three lineons are created or annihilated. This includes, as a special case, a single straight line, meaning that fully polarized chains can be flipped at zero energy cost. For a system with periodic boundaries, this corresponds to sending a single spinon around a non-contractible handle of the torus. Figure 6(b) illustrates a cage which includes a non-contractible winding. These structures correspond precisely

<sup>6</sup> The term lineon refers to a quasiparticle confined to a line, planeon refers to a quasiparticle confined to a plane, and fracton refers to a quasiparticle that cannot move (confined to a point). However, the term “fracton” is often used loosely to refer to any type of sub-dimensional quasiparticle.

to the generalized Wilson loops of fracton gauge theories [84]. Thus, they give rise to a fracton CSL—a classical *cage-net condensate* [64].

### B. Thermodynamics from Cluster Monte Carlo

Having established the vacuum-to-vacuum “tunneling” processes characterizing this putative CSL, it remains to demonstrate the thermodynamic stability of the underlying Ising model against the development of any ordering instabilities. This means that the system possesses a non-zero ground state entropy, does not undergo any finite-temperature ground state selection by an order-by-disorder mechanism, and exhibits algebraically decaying correlations. Demonstrating these properties requires performing a Monte Carlo simulation of the statistical Boltzmann distribution. As is the general case with Ising models, single spin flip Markov chain updates face exponentially small acceptance rates at low temperature. This problem is doubly compounded in the present fracton spin liquid by the highly correlated sequence of spin flips required to achieve a vacuum-to-vacuum cage move. In an ice model, one only pays the price of creating a pair of spinons, after which they can undergo diffusive random walks at zero energy cost until they meet again and annihilate. In the fracton CSL, a single spin flip creates two lineons, which cannot move off of a chain; instead, they can only be split as in Fig. 5(c), costing additional energy. Even after a number of lineons are created, they can only be recombined if their associated lines intersect in trios, to form a cage net such as those in Fig. 6(a,b). This makes single spin flip Monte Carlo untenable for low-temperature simulation.

To overcome this problem, we have developed a highly efficient cluster algorithm capable of generating cage-nets like the one shown in Fig. 6(b). The algorithm is based on the method of graph decomposition introduced by Otsuka for constructing string-nets to simulate spin ice [59]. In order to construct cage-nets, the algorithm operates by “breaking up” each octahedron into straight segments, corners, or endpoints, designed to decompose each spin configuration into networks of straight strings which may either terminate in trios or have open ends. At zero temperature, only closed cage-nets can be created, such as the one shown in Fig. 6(b), while at finite temperatures these cages can have open ends, creating or destroying lineons. Details of the algorithm are provided in Appendix F.

The thermodynamic results of the simulations using the cluster algorithm are presented in Fig. 6(c), which shows the temperature dependence of the specific heat and entropy. The specific heat exhibits a Shottky-like maximum near  $T/J \sim 1$ , corresponding to the depopulation of lineon quasiparticles at low temperatures. We find no signature of any anomaly that could suggest a phase transition, with the specific heat curve exhibiting no quantitative changes with system size, as shown in the inset. The entropy, obtained by integrating the specific heat (Appendix F), demonstrates extensive degeneracy at zero temperature, with a rather large entropy per spin of  $\approx 0.1176(2)$ . For comparison, we also compute a Pauling-type estimate as follows: viewed as a vertex model on the cu-

bic lattice with  $2^6 = 64$  total allowed vertex configurations, the ground states allow 10 vertex configurations (eight  $T_{1g}$  ground states plus two  $A_{1u}$  ground states); treating these constraints as independent, the Pauling estimate of the number of ground states of the entire system is  $\Omega \approx 2^{N_e} (10/64)^{N_v}$ , where  $N_e$  is the number of edges (equal to the number of spins) and  $N_v$  is the number of vertices (equal to a third of the number of spins), giving an estimate of the zero-temperature entropy per spin of  $\ln \Omega/N_e \approx 0.074$ .<sup>7</sup>

### C. Rank-2 Tensor Spin Liquid: U(1) X-cube Model

By writing the Hamiltonian as in Eq. (10), it is clear that the ground states satisfy a local microscopic constraint on each octahedron  $o$ ,

$$Q_o^{\alpha\alpha} = 0, \quad (15)$$

for each  $\alpha$  (recall that  $Q^{\alpha\beta} = 0$  for  $\alpha \neq \beta$ ). We can alternatively re-express the three diagonal components of  $Q$  as the  $x^2 - y^2$  and equivalent quadrupole moment components in the three planes,

$$\begin{aligned} q_o^z &= Q_o^{xx} - Q_o^{yy}, \\ q_o^y &= Q_o^{zz} - Q_o^{xx}, \\ q_o^x &= Q_o^{yy} - Q_o^{zz}. \end{aligned} \quad (16)$$

These are not linearly independent,  $\sum_\alpha q_o^\alpha = 0$ , reflecting  $\text{Tr}[Q] = 0$ , and so form an over-complete basis for the two  $E_u$  degrees of freedom, but with the advantage that the three directions are treated equivalently. Explicitly, in the primitive 3-site unit cell where  $S_i^z > 0$  corresponds to a moment pointing along the positive Cartesian axis directions, these can be written as

$$q_o^z = [S^z(\mathbf{r}_o + \delta\hat{x}) - S^z(\mathbf{r}_o - \delta\hat{x})] - [S^z(\mathbf{r}_o + \delta\hat{y}) - S^z(\mathbf{r}_o - \delta\hat{y})], \quad (17)$$

and similarly for the other two, where  $\mathbf{r}_o$  is the location of the center of the octahedron and  $\delta$  is the distance from the center of an octahedron to a corner. If  $S^z(\mathbf{r}_o \pm \delta\hat{x}) > 0$  then the magnetic moments point in the  $+\hat{x}$  direction, and similarly of the other two directions. This, identifying the  $S_i^z$  operators on the three sublattices with magnetic moments along the three axes, and coarse-graining by taking the limit  $\delta \rightarrow 0$ , we obtain the following three Gauss laws relating the quadrupolar charge density  $\mathcal{Q}$  to the continuum dipole field  $\mathcal{D}$ ,

$$\begin{aligned} \mathcal{Q}_z &= \partial_x \mathcal{D}_x - \partial_y \mathcal{D}_y, \\ \mathcal{Q}_y &= \partial_z \mathcal{D}_z - \partial_x \mathcal{D}_x, \\ \mathcal{Q}_x &= \partial_y \mathcal{D}_y - \partial_z \mathcal{D}_z. \end{aligned} \quad (18)$$

<sup>7</sup> The Pauling entropy is expected to give a lower bound on the ground state entropy because it overcounts the single-vertex constraints by treating them as independent, while some constraints are redundant when considering larger clusters. Corrections could be obtained systematically through the so-called numerical linked cluster expansion (NLCE) [85].

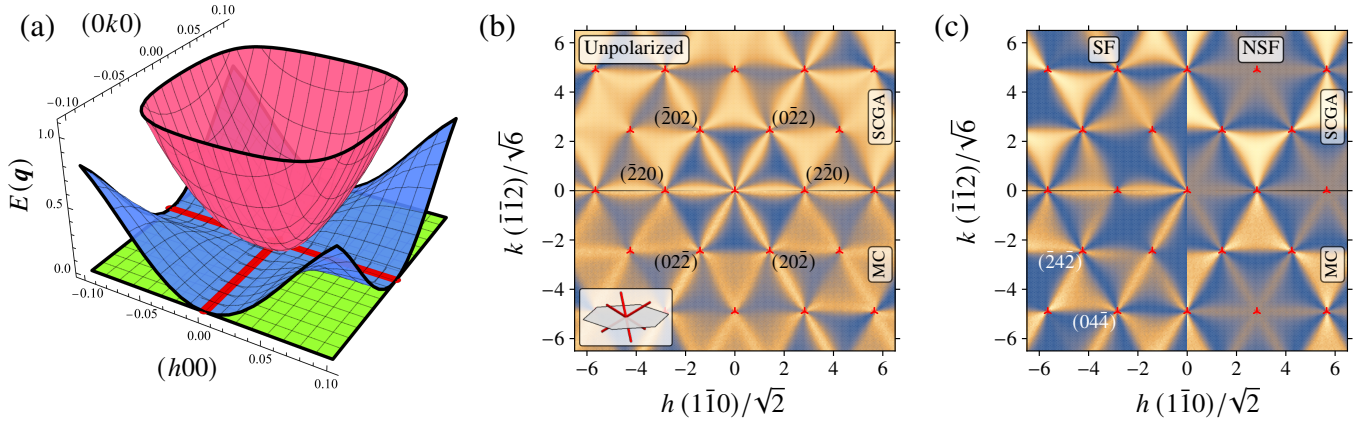


FIG. 7. **X-cube as pinch line spin liquid.** (a) The long-wavelength band structure of the interaction matrix for the fracton X-cube spin liquid, with one flat band (green) and two dispersing bands (blue, red). All three touch at the zone center, while one dispersive band (blue) touches the flat band along the  $\{00h\}$  lines, making this a pinch line spin liquid [28, 30]. (b) Unpolarized neutron scattering structure factor in the reciprocal space plane orthogonal to the  $(111)$  direction,  $\mathbf{q} = h(\bar{1}\bar{1}0)/\sqrt{2} + k(\bar{1}\bar{1}2)/\sqrt{6}$ . This plane cuts through the intersection points of the pinch lines as shown in the inset, revealing a multifold pinch point scattering pattern with pinch points at  $\mathbf{q}$  with  $h = n\sqrt{2}$ ,  $k = m\sqrt{6}$ ,  $n, m \in \mathbb{Z}$ . Reciprocal space indices are given in units of  $2\pi/a_0$  with  $a_0$  the edge length of the 24-site cubic conventional cell (Appendix A). (c) Further refinement of the cross section into polarized scattering channels—spin flip (SF) and non-spin-flip (NSF) (Appendix E). Both (b) and (c) show structure factors obtained with the self-consistent Gaussian approximation (SCGA, top half, Appendix D) and Monte Carlo simulations (MC, bottom half).

These three constraints can be put in the form of a rank-2 tensor gauge theory by rearranging the components of the dipole moment vector field into a hollow symmetric rank-2 tensor “electric” field  $\mathcal{E}$ , and writing the Gauss constraint as

$$q_\alpha = \epsilon_{\alpha\beta\gamma} \partial_\beta \mathcal{E}_{\gamma\alpha} = 0 \quad \text{with} \quad \mathcal{E} = \begin{pmatrix} 0 & \mathcal{D}_z & \mathcal{D}_y \\ \mathcal{D}_z & 0 & \mathcal{D}_x \\ \mathcal{D}_y & \mathcal{D}_x & 0 \end{pmatrix}, \quad (19)$$

where only  $\beta$  and  $\gamma$  are contracted. If we sum over  $\alpha$  we find that  $\sum_\alpha q_\alpha = 0$ , reflecting that analogous microscopic constraint and showing that there are only two linearly independent charges—the two components of the  $E_u$  quadrupole moment.

The Gauss law Eq. (19) is known to describe the field theory of the U(1) X-cube model [62, 78, 86, 87]. The quantum X-cube model [62] is a minimal model realizing  $\mathbb{Z}_2$  fracton topological order, generalizing the  $\mathbb{Z}_2$  toric code model which realizes Abelian topological order [88]. The three linearly-dependent constraints which enforce zero  $x^2 - y^2$ ,  $y^2 - z^2$ , and  $z^2 - x^2$  quadrupole moments, Eqs. (15) and (16), are the U(1) versions of the three “star operators” per vertex appearing in the  $\mathbb{Z}_2$  version of the X-cube model [62]. In the  $\mathbb{Z}_2$  X-cube model, spin flips violate two of the three star stabilizers, creating lineon quasiparticles restricted to move in one direction [62]. The linear dependence of these three Gauss operators enforces that these quasiparticles annihilate in trios [89]. In our classical model, flipping a spin along the  $z$  axis generates  $q_0^x \neq 0$  and  $q_0^y \neq 0$  on the two neighboring octahedra; each of these quasiparticles therefore carries  $z^2 - x^2$  and  $z^2 - y^2$  quadrupolar charge, which sum to an overall  $\pm(3z^2 - r^2)$  quadrupolar charge. As we demonstrated previously, these are lineon quasiparticles which are constrained to move along the  $z$  axis. As far as we are aware, it has not previously been clearly stated

that the lineon quasiparticles of the X-cube model carry  $E_u$  quadrupolar charge (though it is indirectly implied by the field theory construction of Ref. [86] based on irreps of a cubic subgroup of  $\text{SO}(3)$ ).

#### D. Pinch Lines and Neutron Scattering Diagnostics

Classical spin liquids are usually associated with a set of zero-energy flat bands in the spectrum of the interaction matrix sharing a topological band touching with the dispersing bands [17–19, 23, 90]. The flat bands give rise to characteristic diffuse patterns in reciprocal space structure factors, while the band touchings give rise to “pinched” singular features reflecting power-law decay correlations in direct space [56, 70]. These pinched features are experimentally detectable in neutron scattering experiments, and can be resolved most clearly using polarization analysis, as was famously done in the compound  $\text{Ho}_2\text{Ti}_2\text{O}_7$  [11].

The bands of the interaction matrix of Eq. (10) are shown in Fig. 7(a), in the  $\mathbf{q} = (hk0)$  plane in the vicinity of the zone center (Appendix C). One of three bands (green) is flat, with both dispersing bands touching it at the zone center. The fact that two of the three bands are dispersive is in agreement with the fact that there are two linearly independent microscopic constraints, Eq. (15), per primitive unit cell. One of the dispersing bands (blue) has a line degeneracy with the flat band along the  $\{00h\}$  axes of reciprocal space, a situation referred to as a “pinch line spin liquid” [28, 30].

Like some other known examples [23, 29], the full structure of the pinch features is not reflected in the spin structure factor  $S(\mathbf{q})$ , i.e. the Fourier transform of  $\langle S_i^z S_j^z \rangle$ . However, their signatures are visible in neutron scattering structure factors,

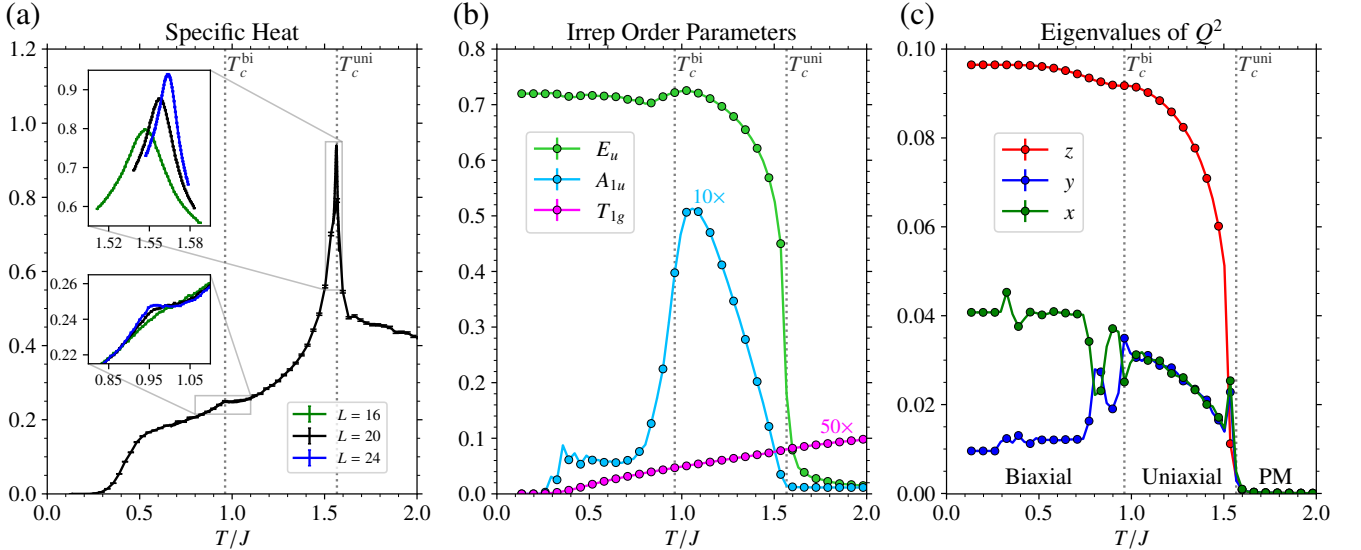


FIG. 8. **Specific heat and order parameters in the  $E_u \wedge A_{1u}$  spin nematic phase.** Here we show thermodynamic data obtained from Monte Carlo simulation at the point directly opposite to the X-cube CSL denoted “fully packed fractons” in Fig. 1(f). This point is representative of the behavior we find in the entire phase. (a) Specific heat, showing a sharp anomaly at the higher-temperature critical temperature  $T_c^{\text{uni}}$ , and a much weaker anomaly at  $T_c^{\text{bi}}$ . At the lowest temperatures, the specific heat decays to zero, and we are able to fit it to the exact solution for finite 1D chains. (b) Magnitudes of the multipole order parameters, Eqs. (11) to (13), note the  $A_{1u}$  order parameter is scaled by  $10\times$  and the  $T_{1g}$  order parameter scaled by  $50\times$ . The quadrupolar  $E_u$  order parameter grows rapidly at  $T_c^{\text{uni}}$ , and the  $A_{1u}$  order parameter grows with it due to an allowed coupling in the Landau free energy, Eq. (21). Below  $T_c^{\text{bi}}$ , the  $E_u$  order parameter exhibits system-size-dependent non-monotonicities, and the  $A_{1u}$  order parameter decays rapidly. (c) Squares of eigenvalues of the quadrupole tensor order parameter,  $\langle(Q^{\alpha\alpha})^2\rangle$ ,  $\alpha \in \{x, y, z\}$  [Eq. (13)], which clearly demonstrate that the intermediate phase is uniaxial, with two eigenvalues degenerate, and the low-temperature phase is biaxial, with three distinct eigenvalues. Simulations are performed with the 24-site unit cell (Appendix A), simulation details are provided in Appendix F.

which refine the spin structure factor by weighting the contribution from different sublattices inequivalently depending on the wavevector  $\mathbf{q}$  (Appendix E). They appear as singular features along a grid of lines in reciprocal space parameterized as  $\{2n, 2m, l\}$ , where  $n, m$  are integers and  $l$  varies continuously. The easiest way to detect the pinch line structure is to take a reciprocal space cut in the plane orthogonal to the (111) direction, because this plane cuts through the zone centers where three pinch lines intersect, without containing any pinch lines in the plane. This is illustrated in the inset of Fig. 7(b). We compute the unpolarized neutron structure factor assuming perfectly Ising moments (Appendix E) in this plane using both the Gaussian approximation (Appendix D) and Monte Carlo, shown in Fig. 7(b). This reveals a characteristic pinch point pattern, including multi-fold pinches characteristic of higher-rank spin liquids [91]. Further refinement is in principle possible using polarization techniques [11]; Fig. 7(c) shows the calculation spin-flip (SF) and non-spin-flip (SF) channel cross sections.

This concludes our study of the X-cube CSL. While this spin liquid has zero-energy flat bands with a flat line touching, we turn next to the opposite side of the phase diagram where the interaction matrix exhibits zero-energy flat lines. Zero-energy flat lines suggest the possibility of subextensive ground state degeneracies, and corresponding frustrated physics intermediate between spin liquids and ordered phases.

## VI. $E_u \wedge A_{1u}$ SPIN NEMATIC PHASE

We turn now to the final part of the phase diagram, the  $E_u \wedge A_{1u}$  phase, indicated by the blue-green hatched arc on the bottom right of the phase diagram in Fig. 1(f). While it is not a spin liquid, hosts exhibits remarkable frustrated behavior intermediate between spin liquidity and long-range-order owing to a subextensive ground state degeneracy. The single-octahedron ground states are the quadrupolar-plus-monopolar configurations in Fig. 2(b) which maximize the  $E_u$  quadrupole moment. In particular, this phase contains the point directly opposite to the X-cube fracton CSL point, whose Hamiltonian is  $-\tilde{H}_{\text{X-cube}}$  [Eq. (10)]. This point is denoted by the label “fully packed fractons” in Fig. 1(f), since its ground states can be described as a maximal packing on X-cube lineons, i.e. a “fracton crystal”, in direct analogy to the interpretation of the AIAO phase as a monopole crystal [66].

### A. Two Transitions: Uniaxial and Biaxial Spin Nematics

Performing single spin flip Monte Carlo simulations throughout this phase, we identify a clear phase boundary when cooling from the high-temperature paramagnetic phase, signaled by a prominent, sharp peak in the specific heat. The corresponding transitions temperatures are marked in the phase diagram Fig. 1(f). The maximum critical temperature

occurs near the “fully packed fracton” point; the thermodynamic behavior at this point is qualitatively representative of the behavior across the entire phase, so we use it to illustrate.

Figure 8(a) shows the specific heat as a function of temperature at this point, exhibiting a very prominent peak at  $T_c^{\text{uni}}/J \approx 1.56$ . The inset demonstrates system size scaling of the peak, showing characteristics of a continuous transition. Figure 8(b) shows that at this temperature the magnitude of  $E_u$  quadrupole tensor order parameter,  $\text{Tr}[Q]^2$  where  $Q$  is defined in Eq. (13), activates rapidly. The monopolar  $A_{1u}$  order parameter, Eq. (11), also activates in tandem, though the magnitude of the  $A_{1u}$  order parameter is small relative to the  $E_u$  order parameter; note that it is scaled by a factor of 10 for visibility. The dipolar order parameter, Eq. (12), remains near zero; note that it is scaled by a factor of 50 for visibility. The activation of the  $E_u$  order parameter indicates long-range quadrupolar order and breaking of lattice rotation symmetry. We therefore characterize the phase below this transition as a spin nematic.

At lower temperature, we identify a second phase transition near  $T_c^{\text{bi}}/J \approx 0.96$ . It is signaled by a small peak in the specific heat, which is only clearly resolvable for relatively large system sizes, highlighted in the inset of Fig. 8(a). Below this transition, we observe non-monotonic behavior in the  $E_u$  order parameter, shown in Fig. 8(b). Just above this transition, the  $A_{1u}$  order parameter reaches a peak and begins to rapidly decline, though it varies smoothly through the transition itself. At the lowest temperatures, the specific heat eventually decays to zero.

The nature of these two low-temperature phases is exposed by examining the three eigenvalues of the quadrupole tensor. This is particularly straightforward in the present case because the  $E_u$  part of the tensor is diagonal. Figure 8(c) shows the thermal expectation values of the squares of the diagonal elements  $\langle(Q^{\alpha\alpha})^2\rangle$ , which are non-negative and so simpler to measure while still containing the relevant information. In the paramagnetic phase, all eigenvalues are zero. In the intermediate temperature phase, two of the three eigenvalues are degenerate, indicating that the system exhibits uniaxial nematic order. In the lowest temperature phase, the two degenerate eigenvalues split, indicating that the system develops biaxial nematic order. These behaviors are most cleanly demonstrated by extracting the two linearly independent components of the quadrupolar order parameter,

$$Q_{3z^2-r^2} = \frac{2Q^{zz} - Q^{xx} - Q^{yy}}{\sqrt{6}}, \quad Q_{x^2-y^2} = \frac{Q^{xx} - Q^{yy}}{\sqrt{2}}, \quad (20)$$

At  $T_c^{\text{uni}}$ ,  $Q_{3z^2-r^2}$  becomes non-zero, indicating that the uniaxial director is along the  $z$  axis, reducing the lattice rotational symmetry to tetragonal. Because the remaining two eigenvalues are degenerate,  $Q_{x^2-y^2}$  remains zero. At  $T_c^{\text{bi}}$ , the two degenerate eigenvalues split, and  $Q_{x^2-y^2}$  becomes non-zero, signaling the development of a second direct axis, further reducing the symmetry to orthorhombic.

## B. Uniaxial Nematic Phase Transition

The high-temperature phase transition at  $T_c^{\text{uni}}$  to uniaxial nematic order is characterized by the activation of the  $E_u$  and  $A_{1u}$  order parameters, so it should naturally be described within the Landau symmetry breaking paradigm. In terms of the monopole and quadrupole order parameters Eqs. (11) and (13), the minimal free-energy functional is

$$F[\phi, Q] = r_E \text{Tr}[Q^2] + r_A \phi^2 + w \phi \text{Tr}[Q^3] + g \phi^2 \text{Tr}[Q^2] + u_A \phi^4 + u_E \text{Tr}[Q^2]^2 + \dots \quad (21)$$

where the ellipses denote terms involving the  $T_{1g}$  dipole order parameter, Eq. (12), as well as sixth-order and higher terms.<sup>8</sup> Note that, unlike a nematic liquid crystal, a cubic term  $\text{Tr}[Q^3]$  is forbidden in the free energy expansion because it transforms in the non-trivial  $A_{1u}$  irrep, owing to the fact that the underlying degrees of freedom are angular momenta. This gives the possibility of a continuous second-order phase transition, which appears consistent with the data in Fig. 8(b). The fact that the nematic order is uniaxial is consistent with the general observation that biaxial nematic orders are quite rare; indeed, in the fourth-order Landau free energy functional above with  $r_E < 0$ , the minima always correspond to uniaxial orders, which have  $\text{Tr}[Q^3] \neq 0$ . Pure biaxial orders, which have  $\text{Tr}[Q^3] = 0$ , are only selected by tuning an irrelevant sixth-order  $\text{Tr}[Q^3]^2$  term.

The linear-cubic term  $\phi \text{Tr}[Q^3]$ , which couples the two monopole and quadrupole order parameters, is allowed by symmetry. In particular,  $w \neq 0$  means that when the  $E_u$  order parameter activates,  $\text{Tr}[Q^3]$  acts as a conjugate field turning on the  $A_{1u}$  as a secondary (induced) order parameter, even if  $r_A > 0$  at the transition. This is perfectly consistent with our measurements in Fig. 8(b)—the magnitude of the  $A_{1u}$  order parameter remains very small, an order of magnitude less than the primary  $E_u$  order parameter.

Before continuing, it is worth mentioning that we could alternatively define a two-component vector order parameter for the  $E_u$  irrep using Eq. (20), or equivalently a single complex order parameter,

$$\tilde{q} = Q_{3z^2-r^2} + iQ_{x^2-y^2} = |\tilde{q}|e^{i\vartheta}. \quad (22)$$

In terms of  $\tilde{q}$ , we can rewrite the quadrupole tensor invariants as  $\text{Tr}[Q^2] = |\tilde{q}|^2$  and  $\text{Tr}[Q^3] = |\tilde{q}|^3 \cos(3\vartheta)/\sqrt{6}$ . The six pure-uniaxial  $\pm(3\alpha^2 - r^2)$  configurations correspond to  $\vartheta \in \mathbb{Z}\pi/3$ , while the six pure-biaxial  $\pm(\alpha^2 - \beta^2)$  configurations with  $\text{Tr}[Q^3] = 0$  correspond to  $\vartheta \in (\mathbb{Z} + 1/2)\pi/3$  ( $\alpha, \beta \in \{x, y, z\}$ ). This free energy is then formally equivalent to that describing the development of so-called “ $\psi_2$ ” (uniaxial) and “ $\psi_3$ ” (biaxial) orders in anisotropic pyrochlore

<sup>8</sup> Up to fourth order the only allowed  $T_{1g}$  couplings are  $r_T|\mathbf{D}|^2$ ,  $u_T|\mathbf{D}|^4$ ,  $g'|\mathbf{D}|^2\phi^2$ ,  $g''|\mathbf{D}|^2\text{Tr}[Q^2]$ , with no linear-cubic couplings. We expect both  $r_A, r_T > 0$  at the transition since these irreps are gapped in the microscopic Hamiltonian, but with  $r_A \ll r_T$  since the  $2z^2 - r^2$  single-octahedron fragmented ground state configurations, Fig. 2(b), carry an  $A_{1u}$  component.

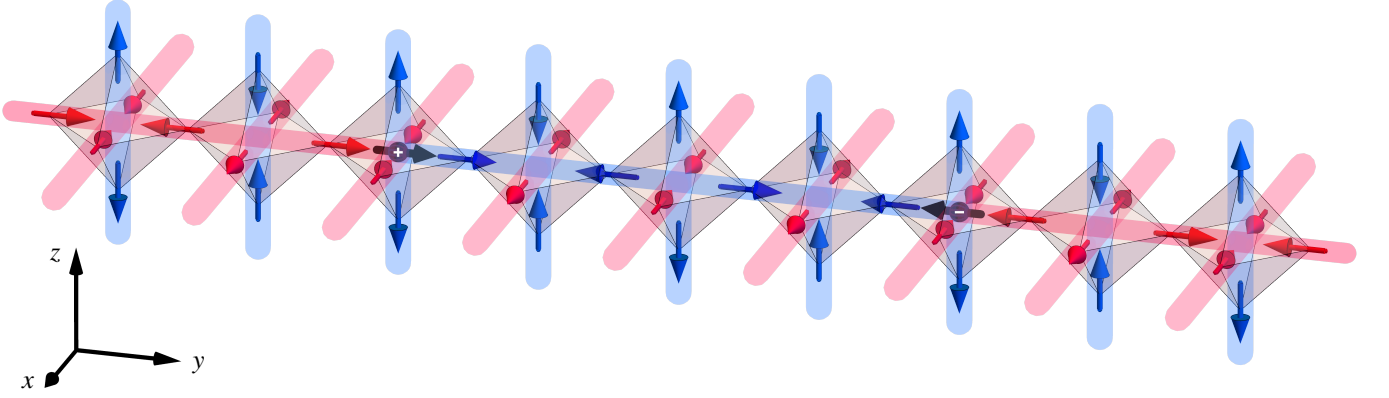


FIG. 9. **Deconfined AFM spinons in the biaxial nematic phase.** The low-temperature biaxial nematic phase of the  $E_u \wedge A_{1u}$  quadrant of the phase diagram is entropically stabilized by deconfined 1D AFM spinons. Here we demonstrate for a single chain. Consider first Neél-polarizing all  $z$ -chains with  $\mathcal{N}_c = +1$  (blue tubes) and all  $x$ -chains with  $\mathcal{N}_c = -1$  (red tubes). Each  $y$ -chain then has two possible ground states, either  $\mathcal{N}_c = \pm 1$ . Domain walls between the two Neél domains on a  $y$ -oriented chain are deconfined antiferro-spinons. These are indicated by short black arrows since they carry a conserved (staggered) dipole moment,  $\mathbf{D}_o$  in Eq. (3). These antiferro-spinons are free to hop along the chain by flipping one spin at a time at zero energy cost, thus they can keep the chain disordered at any positive temperature, maximizing entropy and minimizing free energy.

spin models [3, 4, 92, 93], in which activation of the scalar order parameter has also been observed to occur by the same linear-cubic coupling [93].

Microscopically, it is useful to consider a particular representative microstate, constructed by copying the fragmented  $(2z^2 - r^2)$  configuration from Fig. 2(b) to every A octahedron. In the resulting state, every B octahedron is in the time-reversed  $-(2z^2 - r^2)$  configuration. This is, therefore, a ground state of the spin nematic phase and we refer to it as the *global*- $(2z^2 - r^2)$  state. This state has large  $E_u$  and  $A_{1u}$  order parameters and, in particular, it maximizes  $Q_{3z^2 - r^2}$  while having  $Q_{x^2 - y^2} = 0$ , so is a purely uniaxial state. It can be thought of as a representative for the type of uniaxial-plus-monopolar order realized in the intermediate phase, disordered by the presence of excited octahedra. The lowest-energy excited state in this phase is the  $E_u \wedge T_{1g}$  configuration shown in Fig. 2(a), which has zero  $A_{1u}$  moment. The presence of a large fraction of these defective octahedra suppresses the  $A_{1u}$  moment, explaining why the  $A_{1u}$  order parameter is significantly weaker than the  $E_u$  order parameter. A typical microstate in the uniaxial phase may be viewed as the *global*- $(2z^2 - r^2)$  state, disordered by excited octahedra primarily in the  $E_u \wedge T_{1g}$  configurations, plus randomly oriented  $\pm(2x^2 - r^2)$  and  $\pm(2y^2 - r^2)$  octahedra.

### C. Fluctuation-Driven Biaxial Dimensional Reduction

The lower-temperature phase transition at which the biaxial  $Q_{x^2 - y^2}$  component of the order parameter activates is significantly more complex. We argue here that it is driven by a fluctuation mechanism similar to order-by-disorder, which selects a state in which a set of chains in one direction are maximally disordered by deconfined antiferro-spinons.

To show this, we first demonstrate that there are a subextensive number of ground states. Using the 3-site unit cell (Appendix A), we define a chain-based Neél order parameter

for each chain  $c$ ,

$$\mathcal{N}_c = (-1)^c \frac{1}{L} \sum_{i \in c} (-1)^i S_i^z \quad (3\text{-site unit cell}). \quad (23)$$

The sign  $(-1)^i$  alternates along the chain, thus measuring the staggered magnetization of the chain. The sign  $(-1)^c$  alternates along the two sublattices of the square lattice formed by the chains when viewed along their length. These signs are chosen so that an all-in-all-out configuration corresponds to  $\mathcal{N}_c = +1$  on every chain. Now, consider the *global*- $(2z^2 - r^2)$  uniaxial nematic ground state described above. This state differs from the AIAO state by flipping every chain along the  $x$  and  $y$  axes, i.e. it has  $\mathcal{N}_c = +1$  for  $z$ -oriented chains and  $\mathcal{N}_c = -1$  for  $x$ - and  $y$ -oriented chains. In this state, every chain along the  $x$  direction can be flipped independently without changing the energy, thus giving the system at least  $2^{L^2}$  ground states. Similarly, every chain along the  $y$  direction could also be flipped independently. However, note that flipping an  $x$ -directed chain creates an obstruction to flipping any  $y$ -directed chains which intersect it, as doing so would create an all-in or all-out octahedron at their intersection.

Now, consider fixing the  $z$ -chains to have  $\mathcal{N}_c = +1$  and the  $x$ -chains to have  $\mathcal{N}_c = -1$ , so that each  $y$  chain has two ground states with  $\mathcal{N}_c = \pm 1$ . Flipping a string of spin on a  $y$ -chain creates a pair of domain walls—antiferro-spinons. This is illustrated for a single  $y$ -chain in Fig. 9, where  $z$ -chains with  $\mathcal{N}_c = +1$  are denoted by transparent red tubes, and  $x$ -chains with  $\mathcal{N}_c = -1$ , denoted by transparent blue tubes. The Neél domains on the  $y$ -chain are indicated by blue and red segments, and the domain walls—antiferro-spinons—are denoted with small black arrows indicating the direction of their dipole moment. Like ferro-spinons, these are deconfined quasiparticles which are free to disorder the chain at any finite temperature. These spinons act to disorder the  $y$ -chains and yield a massive finite-temperature entropy and a significant

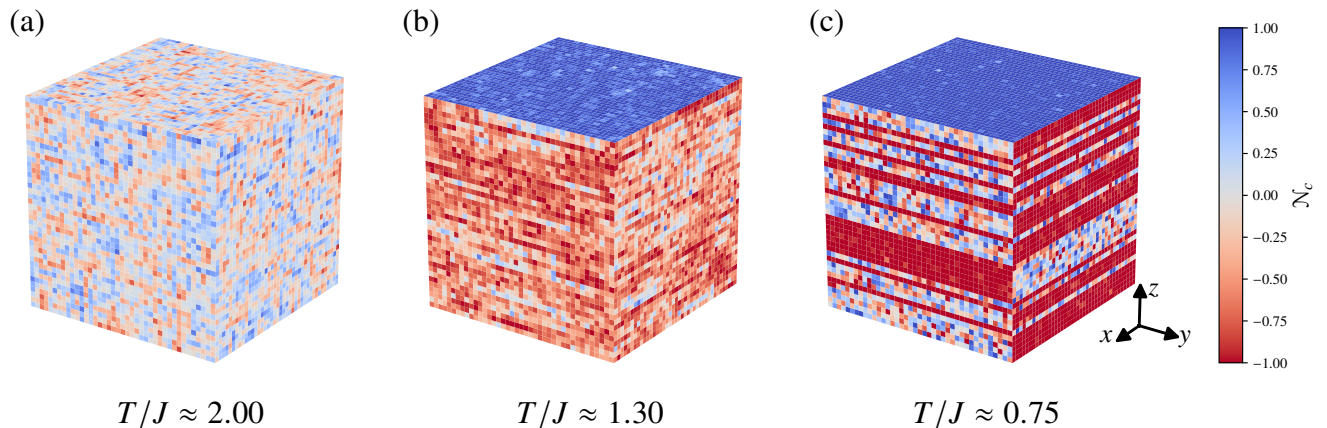


FIG. 10. **Two-stage dimensional reduction.** Here we plot a snapshot of the value of the chain Néel order parameters  $\mathcal{N}_c$ , Eq. (23), where each chain is associated with a point on the surface of a cube. Positive values are denoted in blue and negative values in red, while  $\mathcal{N}_c \approx 0$  is denoted in white. For reference, the two AIAO ground states would have all faces blue or red, respectively, and the global- $(2z^2 - r^2)$  states would have one face opposite the other two. (a) At high temperatures in the paramagnetic phase, all chains are disordered. (b) Just below the transition into the uniaxial phase with tetragonal symmetry, chains along the  $z$ -axis are highly polarized, while chains along the  $x$ - and  $y$ -axes exhibit the opposite and less saturated polarization. (c) Just below the transition into the biaxial phase with orthorhombic symmetry, in each plane orthogonal to the  $z$ -axis, a secondary axis is chosen along which the chains are polarized opposite to the  $z$ -axis polarization, while the remaining axis exhibits disorder due to deconfinement of 1D AFM spinons, see Fig. 9.

reduction in free energy. Thus the transition to biaxial nematic order is driven by the system choosing a secondary axis for ordered AFM chains, so that the chains along the third axis can remain highly disordered. Such a fluctuation-driven mechanism is similar to order-by-disorder, but instead of selecting a particular state out of a large ground state manifold, it instead drives dimensional reduction—the low temperature behavior is that of decoupled 1D chains which remain disordered at finite temperature.

To support this picture, we have measured the Néel polarizations  $\mathcal{N}_c$  in our simulations. Associating each chain to a point on the surface of a cube, we plot the resulting distribution of  $\langle \mathcal{N}_c \rangle$  values in Fig. 10. Blue points indicate chains with  $\langle \mathcal{N}_c \rangle > 0$ , red points indicate chains with  $\langle \mathcal{N}_c \rangle < 0$ , and white chains indicate points with  $\langle \mathcal{N}_c \rangle \approx 0$ . Figure 10(a) shows a snapshot at  $T/J \approx 2.0$ , well into the paramagnetic phase, where all chains are clearly highly disordered,  $\mathcal{N}_c \approx 0$ . Figure 10(b) shows a snapshot at  $T/J \approx 1.3$ , below  $T_c^{\text{uni}} \approx 1.56$  in the intermediate-temperature uniaxial phase. Chains along one direction (without loss of generality, we call it this direction  $z$ ) exhibit a large  $\mathcal{N}_c \approx +1$  (blue face of the cube); the other two directions (call them  $x$  and  $y$ ) show weaker but opposite ordering,  $\mathcal{N}_c \lesssim 0$ . This pattern is consistent with that of the global- $(2z^2 - r^2)$  state (note that the overall sign depends on the sign of the  $A_{1u}$  order parameter  $\phi$ ).

Figure 10(c) shows a snapshot at  $T/J \approx 0.75$ , below  $T_c^{\text{bi}} \approx 0.96$  in the biaxial phase. The situation is more subtle than our explanation above, which would have resulted in the  $z$ -face entirely blue (all  $z$ -chains with  $\mathcal{N}_c = +1$ , the  $x$ -face entirely red (all  $x$ -chains with  $\mathcal{N}_c = -1$ ), and the  $y$ -face mostly white (all  $y$ -chains highly disordered). Instead, upon cooling from the uniaxial phase where the  $z$ -chains are already polarized, the selection of the secondary ordering axis can be

chosen independently in every  $x$ - $y$  plane. In some planes the  $x$ -chains are polarized and the  $y$  chains are disordered, while in other planes the  $y$ -chains are polarized and the  $x$ -chains are disordered, resulting in the “striped” appearance. This is related to what we explained above: starting from the global- $(2z^2 - r^2)$  state, all  $x$ -chains are flippable and all  $y$ -chains are flippable, but flipping an  $x$ -chain obstructs flipping any  $y$ -chain that intersects it and vice-versa. Therefore the deconfinement of antiferro-spinons can happen in only one direction in each  $x$ - $y$  plane, but this direction can be chosen independently in each plane. This is the origin of the non-monotonicity observed in the behavior of the  $E_u$  order parameter below  $T_c^{\text{bi}}$  which are visible in Fig. 8(b). This random ordering could be a consequence of cooling too quickly through the transition in our annealed simulations. We are unable to conclusively determine whether effective inter-plane interactions, mediated by thermal fluctuations flipping spins along the uniaxial director axis, would select a particular pattern of inter-layer ordering if the system were in full thermodynamic equilibrium, and we leave this question for future study.

## VII. DISCUSSION

In this work, we explored the phase diagram of a three-dimensional octochlore lattice with first and second neighbor interactions. In addition to the spin ice string-net CSL with quasiparticle excitations carrying monopole moments [43], in Section V we identified a fracton cage-net CSL with lineon quasiparticle excitations carrying quadrupole moments realizing a classical X-cube model. In Sections IV and VI we also identified two phases with subextensive degeneracies intermediate between spin liquids and ordered phases, whose

low-temperature physics is driven by deconfinement of 1D spinon quasiparticles and corresponding emergent subsystem symmetries. Before concluding, we briefly give an outlook for interesting theoretical directions for future work building on our results. We also give a survey of promising octochlore materials for future experimental directions.

### A. Theoretical Outlook

Our work opens numerous avenues for further research into the physics of 3D frustrated magnets with Ising moments. For one, it would be of interest to explore quantum perturbations of the current octochlore model. The simplest extension is an XXZ model with  $S_i^+ S_j^-$  interactions, but anisotropic  $S_i^+ S_j^+$  and  $S_i^z S_j^+$  terms akin to those on the pyrochlore lattice [94] will be allowed by symmetry as well. In particular, for the X-cube CSL discussed in Section V, it is straightforward to write down a quantum ring exchange term causing tunneling between classical ground states, which performs the cage-net move shown in Fig. 6(a). The resulting effective Hamiltonian will map to a frustrated lattice gauge theory [37, 39], a frustrated version of the U(1) X-cube lattice gauge theory, will give rise to a QSL hosting a photon-like excitation which is gapless along 1D lines in reciprocal space arising from the flat line touching in the band structure [86]. Quantum fluctuations, no doubt, will also give rise to rich sub-dimensional dynamics in both the frustrated chains and spin nematic phases, which will be of great interest to explore.

With regard to the classical model, a number of interesting questions and promising research avenues present themselves. In the frustrated chains phase discussed in Section IV, we did not determine whether a finite-temperature transition occurs. As a problem of statistical mechanics, it is of considerable interest to understand how the spinon collision mechanism drives the transition from a 3D paramagnet. The subextensive chain-based degeneracy is strongly reminiscent of systems with subsystem symmetries, such as the Xu-Moore (or Ising plaquette) model [95, 96] and related models [97]. The Ising plaquette model on the square lattice, defined by a four-spin interaction around every square plaquette, is subsystem symmetric—where flipping each chain individually is an exact  $\mathbb{Z}_2$  symmetry of the Hamiltonian. Those models tend to exhibit glassy behavior at low temperatures [98]. The present model does not have exact subsystem symmetries; rather, it exhibits *emergent* subsystem symmetries in the low-temperature limit. This could yield similar glassy behavior. Thus, one direction for further study is to explore whether the chain polarizations, which appear random, freeze at a finite temperature. In a similar spirit, but with regard to the biaxial spin nematic phase discussed in Section VI, we have not determined whether the direction of the secondary axis is truly random in different planes, or whether weak inter-plane interactions stabilize correlations between them. This might be resolved using low temperature expansion techniques for systems with highly degenerate ground states [99], which would also deepen our understanding of order-by-disorder in classical Ising models, examples of which are sparse.

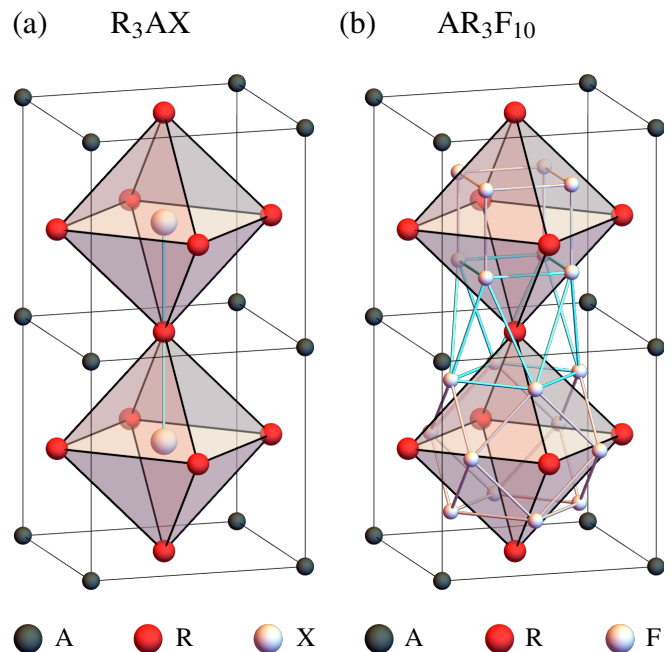


FIG. 11. **Composition of octochlore materials.** (a) The anti-perovskite structure with chemical formula  $R_3AX$ . The R sites form an octochlore lattice. (b) The octochlore fluoride structure with chemical formula  $AR_3F_{10}$  with  $A=K, Rb, Cs$ . The R sites form an octochlore lattice. The R site sits inside of a square anti-prism cage of F ions, shown with cyan lines.

In Section IV C we showed that the two CSLs in the current model can be viewed as condensates of different bound states of spinons arising from coupled chains. This is very similar in spirit to the concept of gauging a subsystem symmetry to generate fracton topological order [100–102]. The spinon bound state condensation approach can be generalized to build Ising CSLs on a variety of lattices constructed from intersecting chains. While the octochlore lattice is the next-simplest after the pyrochlore, it will be very interesting to explore Ising systems on other corner-sharing-cluster lattices with more spins per cluster, giving rise to additional multipole moments, more spin liquids, and more exotic phases intermediate between spin liquids and ordered phases.

### B. Materials and Experimental Outlook

The octochlore structure is perhaps best known in the anti-perovskite (or inverse-perovskite) structure, realized in materials with chemical formula  $R_3AX$  [42]. The R ions form the octochlore lattice as shown in Fig. 11(a), with X ions sitting at the centers of octahedra and A ions in the voids between octahedra. However, anti-perovskites are typically metallic, with a transition metal ion such as Mn occupying the R site [42]. Placing rare-earth ions on the R site of an ideal insulating anti-perovskite is highly unfavorable—their strong preference for the 3+ oxidation state would require unrealistically large negative charge on the A and X ions to maintain charge neu-

trality. Therefore rare-earth anti-perovskites should generally be expected to be metallic. If the  $4f$  moments remain strongly localized and unquenched (weak Kondo coupling), RKKY interaction would naturally generate spin-spin exchange in such materials, though not limited to  $J_1$  and  $J_{2a}$ . Indeed a series of metallic rare earth nitrides  $R_3Ni_n$  with  $R$  a rare earth have been synthesized and characterized [44–46]. One compound in particular,  $Ce_3Ni_n$ , was found to exhibit a transition to commensurate antiferromagnetic order with moments aligned along the crystal axes in Ising-like fashion, apparently with each octahedron in the state shown in Fig. 3(d) [47]. This material and other in the series are therefore an interesting target for further study. While anti-perovskites may not be an ideal place to realize rare earth octochlore *insulators*, they may be a promising platform for *metallic* frustrated magnets, which have generated much interest as platforms for exotic quantum criticality [103, 104] and non-Fermi liquids [105].

A promising family of insulating materials is  $AR_3F_{10}$  [48–54], with  $R$  a trivalent rare earth ion, and  $A=K, Rb, Cs$ , which realize the octochlore structure as shown in Fig. 11(b). Each rare earth ion sits in a square anti-prism cage of  $F$  ions with  $C_{4v}$  symmetry (compare to the distorted cube cage of  $O$  ions with  $D_{3d}$  symmetry surrounding each rare earth ion in pyrochlore oxides [106]). These materials can be grown as single crystals [53, 54]. Chamberlain *et al.* synthesized the  $KR_3F_{10}$  series with  $R=Dy$  [48],  $Er, Yb$  [50], each of which likely exhibit a crystal field ground state doublet with predominantly Ising-like moments ( $KTm_3F_{10}$  may, given its reported thermodynamics [50], have a nearly-degenerate singlet pair). The compounds with  $R=Ho$  [51] and  $Tb$  [54] have a non-magnetic singlet crystal field ground state, but the remaining Lanthanide rare earth compounds in this series remain promising candidates for interesting frustrated magnetic insulators. It is also possible to substitute  $K$  by  $Rb$  [49, 51] or  $Cs$  [53], yielding additional series in the family. In particular the compound  $RbSm_3F_{10}$  has been reported to have Ising moments with no order down to 8 mK [51]. It appears that little further work has been done to study this family as a platform for frustrated magnetism, but the ground work has been laid to explore these compounds in more detail.

Chamberlain *et al.* reports competition between dipole and exchange couplings in the  $KR_3F_{10}$  compounds they studied [48, 50, 51], which may be favorable for observing spin ice physics of dipolar origin [107] in those compounds at low temperatures [43]. In a similar vein as in the current efforts devoted to some rare-earth pyrochlore oxides [3–5], it will be especially interesting to explore whether such compounds with small magnetic moments can be synthesized and whose behavior is governed primarily by exchange couplings, such as potential  $R=Nd$  or  $Ce$  members of the family. While the second-neighbor  $J_{2a}$  exchange may be expected to be weaker than first-neighbor  $J_1$  exchange interaction, for lack of an an-

ion ligand mediating a superexchange pathway, making the realization of the fracton CSL and frustrated chains phase possibly challenging, a positive  $J_1$  with a small  $J_{2a}$  can stabilize either the fragmented spin ice CSL or the spin nematic phase in the phase diagram of Fig. 1(f), either of whose observation would be a significant achievement in the exploration of frustrated magnetic phenomena in three dimensions. Given advances in crystal growth methods which have been applied intensively to grow large clean single crystals of a variety of pyrochlore compounds [108], and growing interest in non-oxide pyrochlores [109], this family of non-oxide octochlore compounds is a promising avenue for the frustrated magnetism experimentalist community to explore.

### C. Conclusion

Altogether, our work lays the groundwork for the exploration of highly frustrated 3D Ising systems beyond the pyrochlore lattice, advancing the theoretical methods for studying these systems and paving the road towards next-generation experimental platforms for studying 3D frustrated magnetism. On the theoretical front, we extend techniques used in the continuous-spin analysis of frustrated magnets to the study of Ising systems, providing a clean demonstration of the utility and physical meaning of the multipolar irreps in the characterization of frustrated phases. We not only identify an elegant classical fracton CSL generalizing the well-known spin ice classical spin liquid, we further establish the existence of remarkable exotic frustrated phases intermediate between spin liquids and conventional long range order. On the experimental front, our work establishes that Ising-like rare-earth magnets in corner-sharing geometries beyond the pyrochlore’s tetrahedra are a highly promising target for further study. We hope our work will inspire the further development and fruitful investigation of both rare-earth anti-perovskite and octochlore fluoride compounds, and spur on the search for other magnetic rare-earth octochlore materials, which may constitute the next generation of 3D frustrated magnets.

### ACKNOWLEDGMENTS

K.T.K.C. thanks Han Yan and Johannes Reuther for useful discussions. The work at the University of Waterloo was funded by the NSERC of Canada. M.D.B. acknowledges CGS-M and CGS-D scholarships from NSERC. M.S. and J.R. were supported by the NSF through grant DMR-2142554. This work was in part supported by the Deutsche Forschungsgemeinschaft under the cluster of excellence ct.qmat (EXC-2147, project number 390858490). This research was enabled in part by computing resources provided by the Digital Research Alliance of Canada.

- delberg, 2011).
- [2] J. S. Gardner, M. J. P. Gingras, and J. E. Greedan, Magnetic pyrochlore oxides, *Rev. Mod. Phys.* **82**, 53 (2010).
  - [3] J. G. Rau and M. J. Gingras, Frustrated Quantum Rare-Earth Pyrochlores, *Annual Review of Condensed Matter Physics* **10**, 357 (2019).
  - [4] A. M. Hallas, J. Gaudet, and B. D. Gaulin, Experimental Insights into Ground-State Selection of Quantum XY Pyrochlores, *Annual Review of Condensed Matter Physics* **9**, 105 (2018).
  - [5] E. M. Smith, E. Lhotel, S. Petit, and B. D. Gaulin, Experimental Insights into Quantum Spin Ice Physics in Dipole–Octupole Pyrochlore Magnets, *Annual Review of Condensed Matter Physics* **16**, 387 (2025).
  - [6] A. P. Ramirez, A. Hayashi, R. J. Cava, R. Siddharthan, and B. S. Shastry, Zero-point entropy in ‘spin ice’, *Nature* **399**, 333 (1999).
  - [7] T. Yavors’kii, T. Fennell, M. J. P. Gingras, and S. T. Bramwell, Dy<sub>2</sub>Ti<sub>2</sub>O<sub>7</sub> Spin Ice: A Test Case for Emergent Clusters in a Frustrated Magnet, *Phys. Rev. Lett.* **101**, 037204 (2008).
  - [8] D. J. P. Morris, D. A. Tennant, S. A. Grigera, B. Klemke, C. Castelnovo, R. Moessner, C. Czternasty, M. Meissner, K. C. Rule, J.-U. Hoffmann, K. Kiefer, S. Gerischer, D. Slobinsky, and R. S. Perry, Dirac Strings and Magnetic Monopoles in the Spin Ice Dy<sub>2</sub>Ti<sub>2</sub>O<sub>7</sub>, *Science* **326**, 411 (2009).
  - [9] M. J. Harris, S. T. Bramwell, D. F. McMorrow, T. Zeiske, and K. W. Godfrey, Geometrical Frustration in the Ferromagnetic Pyrochlore Ho<sub>2</sub>Ti<sub>2</sub>O<sub>7</sub>, *Phys. Rev. Lett.* **79**, 2554 (1997).
  - [10] S. T. Bramwell, M. J. Harris, B. C. den Hertog, M. J. P. Gingras, J. S. Gardner, D. F. McMorrow, A. R. Wildes, A. L. Cornelius, J. D. M. Champion, R. G. Melko, and T. Fennell, Spin Correlations in Ho<sub>2</sub>Ti<sub>2</sub>O<sub>7</sub>: A Dipolar Spin Ice System, *Phys. Rev. Lett.* **87**, 047205 (2001).
  - [11] T. Fennell, P. P. Deen, A. R. Wildes, K. Schmalzl, D. Prabhakaran, A. T. Boothroyd, R. J. Aldus, D. F. McMorrow, and S. T. Bramwell, Magnetic Coulomb Phase in the Spin Ice Ho<sub>2</sub>Ti<sub>2</sub>O<sub>7</sub>, *Science* **326**, 415 (2009).
  - [12] J. G. Rau and M. J. P. Gingras, Magnitude of quantum effects in classical spin ices, *Phys. Rev. B* **92**, 144417 (2015).
  - [13] Thanks to the magnetostatic dipolar interactions, these materials should in principle order at very low temperature [63?], but such order has never been observed experimentally.
  - [14] M. Udagawa and L. Jaubert, eds., *Spin Ice*, Springer Series in Solid-State Sciences, Vol. 197 (Springer International Publishing, Cham, 2021).
  - [15] C. Castelnovo, R. Moessner, and S. L. Sondhi, Magnetic monopoles in spin ice, *Nature* **451**, 42 (2008).
  - [16] C. Castelnovo, R. Moessner, and S. Sondhi, Spin Ice, Fractionalization, and Topological Order, *Annual Review of Condensed Matter Physics* **3**, 35 (2012).
  - [17] H. Yan, O. Benton, R. Moessner, and A. H. Nevidomskyy, Classification of classical spin liquids: Typology and resulting landscape, *Phys. Rev. B* **110**, L020402 (2024).
  - [18] H. Yan, O. Benton, A. H. Nevidomskyy, and R. Moessner, Classification of classical spin liquids: Detailed formalism and suite of examples, *Phys. Rev. B* **109**, 174421 (2024).
  - [19] Y. Fang, J. Cano, A. H. Nevidomskyy, and H. Yan, Classification of classical spin liquids: Topological quantum chemistry and crystalline symmetry, *Phys. Rev. B* **110**, 054421 (2024).
  - [20] D. L. Bergman, C. Wu, and L. Balents, Band touching from real-space topology in frustrated hopping models, *Phys. Rev. B* **78**, 125104 (2008).
  - [21] H. Yan, O. Benton, L. Jaubert, and N. Shannon, Theory of multiple-phase competition in pyrochlore magnets with anisotropic exchange with application to Yb<sub>2</sub>Ti<sub>2</sub>O<sub>7</sub>, Er<sub>2</sub>Ti<sub>2</sub>O<sub>7</sub>, Er<sub>2</sub>Sn<sub>2</sub>O<sub>7</sub>, *Phys. Rev. B* **95**, 094422 (2017).
  - [22] K. T. K. Chung, Mapping the Phase Diagram of a Frustrated Magnet: Degeneracies, Flat Bands, and Canting Cycles on the Pyrochlore Lattice (2024), [arXiv:2411.03429](https://arxiv.org/abs/2411.03429).
  - [23] D. Lozano-Gómez, O. Benton, M. J. P. Gingras, and H. Yan, An Atlas of Classical Pyrochlore Spin Liquids (2024), [arXiv:2411.03547](https://arxiv.org/abs/2411.03547).
  - [24] D. Lozano-Gómez, V. Noculak, J. Oitmaa, R. R. P. Singh, Y. Iqbal, J. Reuther, and M. J. P. Gingras, Competing gauge fields and entropically driven spin liquid to spin liquid transition in non-Kramers pyrochlores, *Proc. Natl. Acad. Sci. U.S.A.* **121**, e2403487121 (2024).
  - [25] V. Noculak, D. Lozano-Gómez, J. Oitmaa, R. R. P. Singh, Y. Iqbal, M. J. P. Gingras, and J. Reuther, Classical and quantum phases of the pyrochlore S=1/2 magnet with Heisenberg and Dzyaloshinskii-Moriya interactions, *Phys. Rev. B* **107**, 214414 (2023).
  - [26] K. B. Yogendra, S. Karmakar, and T. Das, Symmetry, superposition, and fragmentation in classical spin liquids: A general framework and applications to square kagome magnets, *Phys. Rev. B* **110**, L060401 (2024).
  - [27] M. Taillefumier, O. Benton, H. Yan, L. D. C. Jaubert, and N. Shannon, Competing Spin Liquids and Hidden Spin-Nematic Order in Spin Ice with Frustrated Transverse Exchange, *Phys. Rev. X* **7**, 041057 (2017).
  - [28] O. Benton, L. D. C. Jaubert, H. Yan, and N. Shannon, A spin-liquid with pinch-line singularities on the pyrochlore lattice, *Nature Communications* **7**, 11572 (2016).
  - [29] H. Yan, O. Benton, L. D. C. Jaubert, and N. Shannon, Rank-2 U(1) Spin Liquid on the Breathing Pyrochlore Lattice, *Phys. Rev. Lett.* **124**, 127203 (2020).
  - [30] N. Davier, F. A. G. Albarraçín, H. D. Rosales, P. Pujol, and L. D. C. Jaubert, Pinch line spin liquids as layered coulomb phases and applications to cubic models, *Phys. Rev. B* **112**, 104425 (2025).
  - [31] M. Pretko, Generalized electromagnetism of subdimensional particles: A spin liquid story, *Phys. Rev. B* **96**, 035119 (2017).
  - [32] M. Pretko, X. Chen, and Y. You, Fracton phases of matter, *Int. J. Mod. Phys. A* **35**, 2030003 (2020).
  - [33] Y. You, Quantum Liquids: Emergent Higher-Rank Gauge Theory and Fractons, *Annual Review of Condensed Matter Physics* **16**, 83 (2025).
  - [34] M. Pretko, Subdimensional particle structure of higher rank U(1) spin liquids, *Phys. Rev. B* **95**, 115139 (2017).
  - [35] M. Hering, H. Yan, and J. Reuther, Fracton excitations in classical frustrated kagome spin models, *Phys. Rev. B* **104**, 064406 (2021).
  - [36] R. Flores-Calderón, O. Benton, and R. Moessner, Irrational Moments and Signatures of Higher-Rank Gauge Theories in Diluted Classical Spin Liquids, *Phys. Rev. Lett.* **133**, 106501 (2024).
  - [37] M. Hermele, M. P. A. Fisher, and L. Balents, Pyrochlore photons: The U(1) spin liquid in a S = 1/2 three-dimensional frustrated magnet, *Phys. Rev. B* **69**, 064404 (2004).
  - [38] M. J. P. Gingras and P. A. McClarty, Quantum spin ice: A search for gapless quantum spin liquids in pyrochlore magnets, *Rep. Prog. Phys.* **77**, 056501 (2014).
  - [39] K. T. K. Chung and M. J. P. Gingras, 2-form U(1) spin liquids: A classical model and quantum aspects, *Phys. Rev. B* **111**, 064417 (2025).
  - [40] S. T. Bramwell and M. J. Harris, Frustration in Ising-type spin models on the pyrochlore lattice, *Journal of Physics Condensed Matter* **10**, L215 (1998).

- [41] R. Moessner, Relief and generation of frustration in pyrochlore magnets by single-ion anisotropy, *Phys. Rev. B* **57**, R5587 (1998).
- [42] M. Mochizuki, M. Kobayashi, R. Okabe, and D. Yamamoto, Spin model for nontrivial types of magnetic order in inverse-perovskite antiferromagnets, *Phys. Rev. B* **97**, 060401 (2018).
- [43] A. Szabó, F. Orlandi, and P. Manuel, Fragmented Spin Ice and Multi-k Ordering in Rare-Earth Antiperovskites, *Phys. Rev. Lett.* **129**, 247201 (2022).
- [44] M. Kirchner, W. Schnelle, F. R. Wagner, and R. Niewa, Preparation, crystal structure and physical properties of ternary compounds ( $R_3N$ )In,  $R$ =rare-earth metal, *Solid State Sciences* **5**, 1247 (2003).
- [45] R. Niewa, Metal-Rich Ternary Perovskite Nitrides, *European Journal of Inorganic Chemistry*, 3647 (2019).
- [46] F. Alharbi, S. Mehmood, Z. Ali, S. Khan, M. Khan, H. Alqurashi, A. G. Al-Sehemi, S. Trukhanov, M. Silibin, M. Sayyed, D. Tishkevich, and A. Trukhanov, Structure, electronic and magneto-elastic properties of rare earth nitrides  $Ln_3NIn$  ( $Ln = Nd, Pm, Sm, Eu, Gd, Tb$ ) anti-perovskites, *Physica B: Condensed Matter* **695**, 416544 (2024).
- [47] F. Gäbler, W. Schnelle, A. Senyshyn, and R. Niewa, Magnetic structure of the inverse perovskite ( $Ce_3NIn$ ), *Solid State Sciences Molecular Metals, Superconductors and Magnets*, **10**, 1910 (2008).
- [48] S. L. Chamberlain, G. Luo, and L. R. Corruccini, Magnetic ordering in  $KDy_3F_{10}$  A system containing three orthogonal Ising lattices, *Phys. Rev. B* **67**, 134414 (2003).
- [49] S. L. Chamberlain and L. R. Corruccini, Magnetic ordering in  $RbGd_3F_{10}$ , *Journal of Magnetism and Magnetic Materials* **264**, 158 (2003).
- [50] S. L. Chamberlain and L. R. Corruccini, Magnetic ordering in rare-earth fluorides with  $KY_3F_{10}$  structure and axial moments, *Phys. Rev. B* **71**, 024434 (2005).
- [51] S. L. Chamberlain and L. R. Corruccini, Paramagnetic properties of cubic  $RbSm_3F_{10}$  and  $KHo_3F_{10}$ , *Journal of Physics and Chemistry of Solids* **67**, 710 (2006).
- [52] F. You, S. Huang, and Q. Shi, Hydrothermal synthesis of mixed rare earth-alkali metal or ammonium fluorides, *Journal of Rare Earths* **28**, 676 (2010).
- [53] C. D. McMillen, S. Comer, K. Fulle, L. D. Sanjeeva, and J. W. Kolis, Crystal chemistry of hydrothermally grown ternary alkali rare earth fluorides, *Acta Crystallographica Section B* **71**, 768 (2015).
- [54] O. Demortier, S. Petit, B. Fauqué, E. Ressouche, I. Kibalin, J. Robert, R. Sibille, B. Roessli, C. Colin, A. Ivanov, O. Fabelo, T. Fennell, D. Hrabovsky, B. Leridon, F. Le Berre, J. Lhoste, and F. Damay, Unusual planar anisotropy of the induced magnetism in  $KTb_3F_{10}$ , *Phys. Rev. Mater.* **9**, 056201 (2025).
- [55] R. Moessner and J. T. Chalker, Low-temperature properties of classical geometrically frustrated antiferromagnets, *Phys. Rev. B* **58**, 12049 (1998).
- [56] C. L. Henley, The “Coulomb Phase” in Frustrated Systems, *Annual Review of Condensed Matter Physics* **1**, 179 (2010).
- [57] S. R. Sklan and C. L. Henley, Nonplanar ground states of frustrated antiferromagnets on an octahedral lattice, *Phys. Rev. B* **88**, 024407 (2013).
- [58] O. Benton and R. Moessner, Topological Route to New and Unusual Coulomb Spin Liquids, *Phys. Rev. Lett.* **127**, 107202 (2021).
- [59] H. Otsuka, Cluster algorithm for Monte Carlo simulations of spin ice, *Phys. Rev. B* **90**, 220406(R) (2014).
- [60] B. Placke, O. Benton, and R. Moessner, Ising fracton spin liquid on the honeycomb lattice, *Phys. Rev. B* **110**, L020401 (2024).
- [61] N. Niggemann, M. Adhikary, Y. Schaden-Thillmann, and J. Reuther, Classical fracton spin liquid and Hilbert space fragmentation in a 2D spin- $\frac{1}{2}$  model (2025), arXiv:2508.06606 [cond-mat].
- [62] S. Vijay, J. Haah, and L. Fu, Fracton topological order, generalized lattice gauge theory, and duality, *Phys. Rev. B* **94**, 235157 (2016).
- [63] R. G. Melko and M. J. P. Gingras, Monte Carlo studies of the dipolar spin ice model, *J. Phys.: Condens. Matter* **16**, R1277 (2004).
- [64] A. Prem, S.-J. Huang, H. Song, and M. Hermele, Cage-Net Fracton Models, *Phys. Rev. X* **9**, 021010 (2019).
- [65] M. A. Levin and X.-G. Wen, String-net condensation: A physical mechanism for topological phases, *Phys. Rev. B* **71**, 045110 (2005).
- [66] M. E. Brooks-Bartlett, S. T. Banks, L. D. C. Jaubert, A. Harman-Clarke, and P. C. W. Holdsworth, Magnetic-Moment Fragmentation and Monopole Crystallization, *Phys. Rev. X* **4**, 011007 (2014).
- [67] D. A. Huse and A. D. Rutenberg, Classical antiferromagnets on the Kagomé lattice, *Physical Review B* **45**, 7536 (1992).
- [68] E. Lhotel, L. D. C. Jaubert, and P. C. Holdsworth, Fragmentation in Frustrated Magnets: A Review, *Journal of Low Temperature Physics* **201**, 710 (2020).
- [69] D. A. Garanin and B. Canals, Classical spin liquid: Exact solution for the infinite-component antiferromagnetic model on the kagome lattice, *Phys. Rev. B* **59**, 443 (1999).
- [70] C. L. Henley, Power-law spin correlations in pyrochlore antiferromagnets, *Phys. Rev. B* **71**, 014424 (2005).
- [71] A. Danielian, Ground State of an Ising Face-Centered Cubic Lattice, *Physical Review Letters* **6**, 670 (1961).
- [72] C. Wengel, C. L. Henley, and A. Zippelius, Spin-glass and antiferromagnet critical behavior in a diluted fcc antiferromagnet, *Physical Review B* **53**, 6543 (1996).
- [73] T. L. Polgreen, Monte Carlo simulation of the fcc antiferromagnetic Ising model, *Physical Review B* **29**, 1468 (1984).
- [74] R. Stübel and W. Janke, Finite-size scaling of Monte Carlo simulations for the fcc Ising antiferromagnet: Effects of the low-temperature phase degeneracy, *Physical Review B* **98**, 174413 (2018).
- [75] J. Villain, Insulating spin glasses, *Zeitschrift für Physik B Condensed Matter and Quanta* **33**, 31 (1979).
- [76] L. D. C. Jaubert, M. Haque, and R. Moessner, Analysis of a Fully Packed Loop Model Arising in a Magnetic Coulomb Phase, *Phys. Rev. Lett.* **107**, 177202 (2011).
- [77] R. Moessner, Spin Ice As a Coulomb Liquid: From Emergent Gauge Fields to Magnetic Monopoles, in *Spin Ice*, Springer Series in Solid-State Sciences, edited by M. Udagawa and L. Jaubert (Springer International Publishing, Cham, 2021) pp. 37–70.
- [78] K. Slagle and Y. B. Kim, X-cube model on generic lattices: Fracton phases and geometric order, *Phys. Rev. B* **97**, 165106 (2018).
- [79] S. T. Chui, Simple three-dimensional Ising model with finite entropy at zero temperature, *Physical Review B* **15**, 307 (1977).
- [80] D. Tahara, Y. Motome, and M. Imada, Antiferromagnetic Ising Model on Inverse Perovskite Lattice, *Journal of the Physical Society of Japan* **76**, 013708 (2007).
- [81] L.-P. Henry, P. C. W. Holdsworth, F. Mila, and T. Roscilde, Spin-wave analysis of the transverse-field Ising model on the checkerboard lattice, *Physical Review B* **85**, 134427 (2012).
- [82] R. J. Baxter, *Exactly Solved Model in Statistical Mechanics* (Academic Press, London, 1982).

- [83] R. M. Nandkishore and M. Hermele, Fractons, *Annual Review of Condensed Matter Physics* **10**, 295 (2019).
- [84] T. Devakul, S. A. Parameswaran, and S. L. Sondhi, Correlation function diagnostics for type-I fracton phases, *Phys. Rev. B* **97**, 041110 (2018).
- [85] R. R. P. Singh and J. Oitmaa, Corrections to Pauling residual entropy and single tetrahedron based approximations for the pyrochlore lattice Ising antiferromagnet, *Phys. Rev. B* **85**, 144414 (2012).
- [86] N. Seiberg and S.-H. Shao, Exotic U(1) symmetries, duality, and fractons in 3+1-dimensional quantum field theory, *SciPost Physics* **9**, 046 (2020).
- [87] K. Slagle and Y. B. Kim, Quantum field theory of X-cube fracton topological order and robust degeneracy from geometry, *Phys. Rev. B* **96**, 195139 (2017).
- [88] A. Yu. Kitaev, Fault-tolerant quantum computation by anyons, *Annals of Physics* **303**, 2 (2003).
- [89] E. Lake and M. Hermele, Subdimensional criticality: Condensation of lineons and planons in the X-cube model, *Physical Review B* **104**, 165121 (2021).
- [90] N. Davier, F. A. Gómez Albarracín, H. D. Rosales, and P. Pujol, Combined approach to analyze and classify families of classical spin liquids, *Phys. Rev. B* **108**, 054408 (2023).
- [91] A. Prem, S. Vijay, Y.-Z. Chou, M. Pretko, and R. M. Nandkishore, Pinch point singularities of tensor spin liquids, *Phys. Rev. B* **98**, 165140 (2018).
- [92] B. Javanparast, A. G. R. Day, Z. Hao, and M. J. P. Gingras, Order-by-disorder near criticality in XY pyrochlore magnets, *Phys. Rev. B* **91**, 174424 (2015).
- [93] N. Francini, L. Schmidt, L. Janssen, and D. Lozano-Gómez, Exact nematic and mixed magnetic phases driven by competing orders on the pyrochlore lattice (2025), 2510.23704.
- [94] K. A. Ross, L. Savary, B. D. Gaulin, and L. Balents, Quantum Excitations in Quantum Spin Ice, *Phys. Rev. X* **1**, 021002 (2011).
- [95] C. Xu and J. E. Moore, Strong-weak coupling self-duality in the two-dimensional quantum phase transition of  $p + ip$  superconducting arrays, *Phys. Rev. Lett.* **93**, 047003 (2004).
- [96] C. Xu and J. Moore, Reduction of effective dimensionality in lattice models of superconducting arrays and frustrated magnets, *Nuclear Physics B* **716**, 487 (2005).
- [97] M. Mueller, D. A. Johnston, and W. Janke, Exact solutions to plaquette Ising models with free and periodic boundaries, *Nuclear Physics B* **914**, 388 (2017).
- [98] S. Davatollah, D. Dariush, and L. Separdar, Nature of the glassy transition in simulations of the ferromagnetic plaquette Ising model, *Phys. Rev. E* **81**, 031501 (2010).
- [99] J. Slawny, Low-temperature expansion for lattice systems with many ground states, *Journal of Statistical Physics* **20**, 711 (1979).
- [100] W. Shirley, K. Slagle, and X. Chen, Foliated fracton order from gauging subsystem symmetries, *SciPost Physics* **6**, 041 (2019).
- [101] D. J. Williamson and T. Devakul, Type-II fractons from coupled spin chains and layers, *Phys. Rev. B* **103**, 155140 (2021).
- [102] P. Gorantla, A. Prem, N. Tantivasadakarn, and D. J. Williamson, String membrane nets from higher-form gauging: An alternate route to  $\mathbb{P}^2$ -string condensation, *Physical Review B* **112**, 125124 (2025).
- [103] L. Savary, E.-G. Moon, and L. Balents, New Type of Quantum Criticality in the Pyrochlore Iridates, *Phys. Rev. X* **4**, 041027 (2014).
- [104] H. Zhao, J. Zhang, M. Lyu, S. Bachus, Y. Tokiwa, P. Gegenwart, S. Zhang, J. Cheng, Y.-f. Yang, G. Chen, Y. Isikawa, Q. Si, F. Steglich, and P. Sun, Quantum-critical phase from frustrated magnetism in a strongly correlated metal, *Nat. Phys.* **15**, 1261 (2019).
- [105] M. Vojta, Frustration and quantum criticality, *Rep. Prog. Phys.* **81**, 064501 (2018).
- [106] M. A. Subramanian, G. Aravamudan, and G. V. Subba Rao, Oxide pyrochlores — A review, *Progress in Solid State Chemistry* **15**, 55 (1983).
- [107] B. C. den Hertog and M. J. P. Gingras, Dipolar Interactions and Origin of Spin Ice in Ising Pyrochlore Magnets, *Phys. Rev. Lett.* **84**, 3430 (2000).
- [108] M. Powell, L. D. Sanjeeva, C. D. McMillen, K. A. Ross, C. L. Sarkis, and J. W. Kolis, Hydrothermal Crystal Growth of Rare Earth Tin Cubic Pyrochlores,  $\text{RE}_2\text{Sn}_2\text{O}_7$  (RE = La–Lu): Site Ordered, Low Defect Single Crystals, *Crystal Growth & Design* **19**, 4920 (2019).
- [109] D. Reig-i-Plessis and A. M. Hallas, Frustrated magnetism in fluoride and chalcogenide pyrochlore lattice materials, *Phys. Rev. Materials* **5**, 030301 (2021).

### Appendix A: Conventions

The octochlore lattice is the line graph of the cubic lattice, meaning that each octochlore site sits at the midpoint of a cubic lattice edge [56]. Since there are three edges per cubic lattice unit cell we can use a 3-site unit cell with a cubic primitive cell. On the other hand, it is convenient to use a 6-site unit cell which contains all six sites of a single octahedron, with an fcc unit cell. For the purpose of Monte Carlo simulation with periodic boundaries, on the other hand, it is best to use a cubic unit cell, for which we use a larger 24-site unit cell with an enlarged cubic cell. Denoting the Cartesian cubic axis unit vectors  $\hat{x}$ ,  $\hat{y}$ ,  $\hat{z}$ , and general vectors by

$$[abc] \equiv a\hat{x} + b\hat{y} + c\hat{z}, \quad (\text{A1})$$

and  $-[abc] \equiv [\bar{a}\bar{b}\bar{c}]$ , these unit cells have primitive vectors

	<u>3-site</u>	<u>6-site</u>	<u>24-site</u>
$\mathbf{a}_1^{(n)}$	$a_0[\frac{1}{2}00]$	$a_0[\frac{1}{2}\frac{1}{2}0]$	$a_0[100]$
$\mathbf{a}_2^{(n)}$	$a_0[0\frac{1}{2}0]$	$a_0[\frac{1}{2}0\frac{1}{2}]$	$a_0[010]$
$\mathbf{a}_3^{(n)}$	$a_0[00\frac{1}{2}]$	$a_0[0\frac{1}{2}\frac{1}{2}]$	$a_0[001]$

where  $a_0$  is the edge length of the enlarged cubic cell and  $n \in \{3, 6, 24\}$  indicates the number of sites in the unit cell. The sublattice positions for the 3-site unit cell are

$$\mathbf{c}_1^{(3)} = \frac{a_0}{4}[100], \quad \mathbf{c}_2^{(3)} = \frac{a_0}{4}[010], \quad \mathbf{c}_3^{(3)} = \frac{a_0}{4}[001]. \quad (\text{A3})$$

For the 6-site unit cell they are

$$\begin{aligned} \mathbf{c}_1^{(6)} &= \frac{a_0}{4}[100], & \mathbf{c}_2^{(6)} &= \frac{a_0}{4}[010], & \mathbf{c}_3^{(6)} &= \frac{a_0}{4}[001], \\ \mathbf{c}_4^{(6)} &= \frac{a_0}{4}[\bar{1}00], & \mathbf{c}_5^{(6)} &= \frac{a_0}{4}[0\bar{1}0], & \mathbf{c}_6^{(6)} &= \frac{a_0}{4}[00\bar{1}]. \end{aligned} \quad (\text{A4})$$

For the 24-site unit cell, define

$$\bar{\mathbf{c}}_\mu^{(24)} = \mathbf{a}_{\lfloor(\mu-1)/6\rfloor}^{(6)} + \mathbf{c}_{(\mu \bmod 6)+1}^{(6)}, \quad (\text{A5})$$

where  $\mu \in \{1 \dots 24\}$ , we define  $\mathbf{a}_0 \equiv [000]$ , and  $\lfloor \dots \rfloor$  denotes the floor function. This enumerates six corners each for the four octahedra centered at  $\mathbf{a}_0, \mathbf{a}_1^{(6)}, \mathbf{a}_2^{(6)}$ , and  $\mathbf{a}_3^{(6)}$ .

In the 3-site unit cell we define local  $C_{4v}$  easy-axis vectors at each sublattice  $\mathbf{c}_\mu^{(3)}$  as

$$\hat{\mathbf{z}}_1 = [100], \quad \hat{\mathbf{z}}_2 = [010], \quad \hat{\mathbf{z}}_3 = [001], \quad (\text{A6})$$

which point in the positive Cartesian directions. In the 6-site unit cell we define the easy-axis vectors at each sublattice  $\mathbf{c}_\mu^{(6)}$  as

$$\begin{aligned} \hat{\mathbf{z}}_1 &= [100], & \hat{\mathbf{z}}_2 &= [010], & \hat{\mathbf{z}}_3 &= [001], \\ \hat{\mathbf{z}}_4 &= [\bar{1}00], & \hat{\mathbf{z}}_5 &= [0\bar{1}0], & \hat{\mathbf{z}}_6 &= [00\bar{1}], \end{aligned} \quad (\text{A7})$$

such that the six easy-axis vectors point from the center of an octahedron outwards, as in Fig. 1(b), or from the  $A$  to  $B$  sublattices of the bipartite cubic lattice formed by the octahedron centers, see Fig. 1(a).

Given a choice of  $n$ -site unit cell, we consider an  $L \times L \times L$  system with periodic boundaries, for which there are  $L^3$  allowed reciprocal space wavevectors  $\mathbf{q}$  given by

$$\mathbf{q}_{m_1, m_2, m_3} = \frac{1}{L} (m_1 \mathbf{b}_1^{(n)} + m_2 \mathbf{b}_2^{(n)} + m_3 \mathbf{b}_3^{(n)}), \quad (\text{A8})$$

where the  $\mathbf{b}_\alpha^{(n)}$  are reciprocal lattice vectors defined to satisfy  $\mathbf{a}_\alpha^{(n)} \cdot \mathbf{b}_\beta^{(n)} = 2\pi \delta_{\alpha\beta}$ , and  $m_1, m_2, m_3 \in \{0, \dots, L-1\}$ . We define Fourier transforms of single-site variables  $\varphi_i$  as

$$\varphi_\mu(\mathbf{q}) = \frac{1}{\sqrt{L^3}} \sum_{i \in \mu} \varphi_i \exp(-i\mathbf{q} \cdot \mathbf{r}_i) \quad (\text{A9})$$

where  $\mu$  in the sublattice index and we assume system with  $L^3$  unit cells and periodic boundaries. For translationally-invariant two-site variables  $\varphi_{ij}$ , we define the Fourier transform as

$$\varphi_{\mu\nu}(\mathbf{q}) = \frac{1}{L^3} \sum_{i \in \mu} \sum_{j \in \nu} \varphi_{ij} e^{-i\mathbf{q} \cdot (\mathbf{r}_i - \mathbf{r}_j)}. \quad (\text{A10})$$

For specifying reciprocal space wavevectors we use Miller indices with respect to the 24-site unit cell cubic cell,

$$\mathbf{q} = \frac{2\pi}{a_0} (h\hat{\mathbf{x}} + k\hat{\mathbf{y}} + l\hat{\mathbf{z}}) \equiv (hkl). \quad (\text{A11})$$

These are used in Fig. 7.

## Appendix B: Irreps and Multipoles

In the main text we described the phase diagram using irreducible representations of the point group. Here we expand on this. The use of irreps to study the phase diagram of corner-

sharing clusters has seen extensive use in studying nearest-neighbor anisotropic Heisenberg models on the pyrochlore lattice [3, 21–23, 28, 29]. In particular, spin liquids occur when multiple irreps are tuned to be degenerate in the ground state [3, 22, 23, 28, 29]. It works equally well for Ising models, and the octochlore lattice is an excellent platform for its application due to having two inequivalent interactions within the octahedra and thus a rich phase diagram as studied in the main text. The octochlore Hamiltonian we study decomposes into a sum over octahedra

$$H = \frac{1}{2} \sum_{\mathbf{o}} \sum_{\langle ij \rangle \in \mathbf{o}} S_i^z J_{ij} S_j^z, \quad (\text{B1})$$

where the single-octahedron interaction matrix is given using the sublattice ordering convention in Eq. (A7) by

$$J_{ij} = \begin{pmatrix} 0 & J_1 & J_1 & J_{2a} & J_1 & J_1 \\ J_1 & 0 & J_1 & J_1 & J_{2a} & J_1 \\ J_1 & J_1 & 0 & J_1 & J_1 & J_{2a} \\ J_{2a} & J_1 & J_1 & 0 & J_1 & J_1 \\ J_1 & J_{2a} & J_1 & J_1 & 0 & J_1 \\ J_1 & J_1 & J_{2a} & J_1 & J_1 & 0 \end{pmatrix} \quad (\text{B2})$$

The symmetries of the octahedron are described by the group  $O_h$ , which acts on the six Ising spins by permutations of the sublattice position. This 6-dimensional representation  $P$  can be decomposed into irreducible representations, where the number of copies of irrep  $\Gamma$  is given by the formula

$$n_\Gamma = \frac{d_\Gamma}{|O_h|} \sum_{g \in O_h} \chi_\Gamma(g)^* \text{Tr}[P(g)], \quad (\text{B3})$$

where  $g$  are the group elements of  $O_h$ ,  $|O_h| = 48$ ,  $\chi_\Gamma(g)$  is the character (trace) of  $g$  in irrep  $\Gamma$ , and  $d_\Gamma$  is the dimension of the irrep. The result is the decomposition  $P = A_{1u} \oplus E_u \oplus T_{1g}$ . Since Eq. (B2) commutes with all of the  $P(g)$  permutation matrices, its eigenvalues are labeled by  $\Gamma$  and are each  $n_\Gamma$  degenerate. The eigenvalues and eigenvectors are given in Table III, with which the Hamiltonian can be written in the form of Eq. (1).

These irreps correspond to multipole moments of the octahedral spin configuration. Let  $\boldsymbol{\mu}_i = (1/2)g\mu_B S_i^z \hat{\mathbf{z}}_i$  denote the local dipole moment vector. The three-dimensional  $T_{1g}$  irrep describes the net dipole moment of an octahedron,

$$D_0^\alpha = \sum_{i \in \mathbf{o}} \mu_i^\alpha \quad (\text{B4})$$

The other two irreps are contained in the rank-2 moment tensor,

$$M_0^{\alpha\beta} = \sum_{i \in \mathbf{o}} r_i^\alpha \mu_i^\beta \propto \sum_{i \in \mathbf{o}} \hat{\mathbf{z}}_i^\alpha \hat{\mathbf{z}}_i^\beta S_i^z \quad (\text{B5})$$

where  $\mathbf{r}_i$  is the displacement of site  $i$  from the center of the octahedron. The trace of this tensor gives the  $A_{1u}$  irrep order

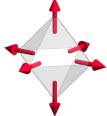
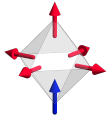
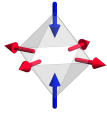
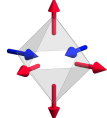
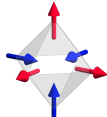
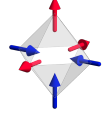
$S^z$	$n$	Configuration	Decomposition
6	(1)		$A_{1u}$
4	(6)		$\frac{2}{3} A_{1u} - \frac{1}{3} E_u + T_{1g}$
	(3)		$\frac{1}{3} A_{1u} - \frac{2}{3} E_u$
2	(12)		$\frac{1}{3} A_{1u} + \frac{1}{3} E_u + T_{1g} + T_{1g}$
	(4)		$T_{1g} + T_{1g} + T_{1g}$
0	(6)		$T_{1g} + E_u$

TABLE II. The decomposition of 32 spin configurations according to the symmetry group of an octahedron. We group the various states by their total  $S^z$  value. The second column shows the degeneracy of these states, and we get the total 64 spin configurations by applying the time-reversal operator. Besides the all-out  $A_{1u}$  monopole, only the  $S^z = 0$  dipole constructed from FM chains transforms as a pure irrep,  $T_{1g}$ .

parameter,

$$\text{Tr}[M_o] \propto \sum_{i \in o} S_i^z = \phi_o, \quad (\text{B6})$$

which may be interpreted as the ‘‘monopole moment’’ of the octahedron since it is a scalar maximized in the all-in-all-out configuration. Note that  $M$  is symmetric. Subtracting its trace we obtain the quadrupole tensor,

$$Q_o^{\alpha\beta} \propto M_o^{\alpha\beta} - \frac{1}{3} \text{Tr}[M_o] \delta^{\alpha\beta} \quad (\text{B7})$$

The off-diagonal elements of this tensor are zero, leaving only two independent degrees of freedom of the trace-free diagonal, forming the two-component  $E_u$  irrep. They correspond to the  $3z^2 - r^2$  and  $x^2 - y^2$  (respectively, the first and second  $E_u$  eigenvectors listed in Table III) components of a quadrupole.

## 1. Irrep Decomposition of Spin Configurations

An octahedron, decorated with Ising spins, has  $2^6 = 64$  different configurations. These split into  $(32 \times 2)$  states and their time-reversal partners and can be further classified according to their total spin and the symmetry group of the octahedron. We collect the 32 spin configurations in Table II, showing their decomposition into the irreducible representations  $A_{1u}$  (monopole),  $E_u$  (quadrupole), and  $T_{1g}$  (dipole).

### Appendix C: Interaction Matrices

Using the 6-site unit cell, the bilinear Hamiltonian Eq. (1) can be written in terms of adjacency matrices of the octochlore lattice,

$$\begin{aligned} H &= \frac{J_1}{2} \sum_{ij} S_i^z A_{ij}^{(1)} S_j^z + \frac{J_{2a}}{2} \sum_{ij} S_i^z A_{ij}^{(2a)} S_j^z \\ &\equiv \frac{1}{2} \sum_{ij} S_i^z \underbrace{[J_1 A_{ij}^{(1)} + J_{2a} A_{ij}^{(2a)}]}_{\mathcal{J}_{ij}} S_j^z, \end{aligned} \quad (\text{C1})$$

where  $A_{ij}^{(n)} = 1$  if sites  $i$  and  $j$  are  $n$ 'th-nearest-neighbors, and 0 otherwise, and the factors of  $1/2$  removes the double counting. We refer to the matrix  $\mathcal{J}_{ij}$  as the interaction matrix. Here, the Ising variables, normalized as  $S_i^z = \pm 1$ , refer to a dipole oriented along the local  $\hat{z}_i$  axis defined in Eq. (A6) and Eq. (A7). This means that  $J_{2a} > 0$  energetically prefers *ferromagnetic* alignment of the dipoles along the 1D chains coupled by the second neighbor interaction.

In the 3-site unit cell, the Fourier transformed adjacency matrices have the form

$$\begin{aligned} A_{\mu\nu}^{(1)}(\mathbf{q}) &= 4 \begin{pmatrix} 0 & s_x s_y & s_x s_z \\ s_x s_y & 0 & s_y s_z \\ s_x s_z & s_y s_z & 0 \end{pmatrix} \\ A_{\mu\nu}^{(2a)}(\mathbf{q}) &= -2 \begin{pmatrix} c_{xx}^+ & 0 & 0 \\ 0 & c_{yy}^+ & 0 \\ 0 & 0 & c_{zz}^+ \end{pmatrix}. \end{aligned} \quad (\text{C2})$$

where  $\mu, \nu$  are sublattice indices and we define

$$s_\alpha \equiv \sin\left(\frac{q_\alpha}{4}\right) \quad \text{and} \quad c_{\alpha\beta}^\pm \equiv \cos\left(\frac{q_\alpha \pm q_\beta}{4}\right). \quad (\text{C3})$$

The negative sign in front of  $A_{\mu\nu}^{(2a)}(\mathbf{q})$  is required because in the 3-site unit cell a positive  $J_{2a}$  prefers anti-ferromagnetic alignment of chains. In the 6-site unit cell the adjacency

matrices are given by

$$A_{\mu\nu}^{(1)}(\mathbf{q}) = 2 \begin{pmatrix} 0 & c_{xy}^- & c_{xz}^- & 0 & c_{xy}^+ & c_{xz}^+ \\ c_{xy}^- & 0 & c_{yz}^- & c_{xy}^+ & 0 & c_{yz}^+ \\ c_{xz}^- & c_{yz}^- & 0 & c_{xz}^+ & c_{yz}^+ & 0 \\ 0 & c_{xy}^+ & c_{xz}^+ & 0 & c_{xy}^- & c_{xz}^- \\ c_{xy}^+ & 0 & c_{yz}^+ & c_{xy}^- & 0 & c_{yz}^- \\ c_{xz}^+ & c_{yz}^+ & 0 & c_{xz}^- & c_{yz}^- & 0 \end{pmatrix}, \quad (\text{C4})$$

$$A_{\mu\nu}^{(2a)}(\mathbf{q}) = 2 \begin{pmatrix} 0 & 0 & 0 & c_{xx}^+ & 0 & 0 \\ 0 & 0 & 0 & 0 & c_{yy}^+ & 0 \\ 0 & 0 & 0 & 0 & 0 & c_{zz}^+ \\ c_{xx}^+ & 0 & 0 & 0 & 0 & 0 \\ 0 & c_{yy}^+ & 0 & 0 & 0 & 0 \\ 0 & 0 & c_{zz}^+ & 0 & 0 & 0 \end{pmatrix} \quad (\text{C5})$$

For the purpose of counting the zero-energy locus of the interaction matrix (after shifting its minimum eigenvalue to zero), as reported in the last column of Table I, one should always use the primitive (3-site) unit cell. The enlarged conventional unit cell yields band folding which multiplies the number of bands.

#### Appendix D: Self-Consistent Gaussian Approximation

The self-consistent Gaussian approximation (SCGA) [69] is a simple soft-spin approximation which works well for computing correlation functions so long as the system remains paramagnetic, in particular for spin liquids. This method replaces the hard spin length constraint  $|S_i^z| = 1$  with a soft one, meaning that the  $S_i^z$  are treated as real-valued variables which vary continuously, with the spin length enforced on average. Given a bilinear spin Hamiltonian

$$H = \frac{1}{2} \sum_{ij} S_i^z \mathcal{J}_{ij} S_j^z \quad (\text{D1})$$

we add a term which energetically regulates the spin length from growing arbitrarily large,

$$H_{\text{SCGA}} = H + \frac{1}{2} \sum_i \lambda_i T (S_i^z)^2, \quad (\text{D2})$$

where the  $\lambda_i$  are to be determined self-consistently by the requirement that  $\langle |S_i^z|^2 \rangle_{\lambda, T} = 1$ , where the angle brackets denote thermal expectation value at fixed  $\lambda$  and temperature  $T$ . The Hamiltonian simplifies to

$$\beta H_{\text{SCGA}} = \frac{1}{2} \sum_{ij} S_i^z (\Lambda_{ij} + \beta \mathcal{J}_{ij}) S_j^z \quad (\text{D3})$$

where  $\beta = 1/T$  is inverse temperature, and  $\Lambda_{ij} = \lambda_i \delta_{ij}$  with  $\delta$  the Kronecker delta. The partition function is then a simple multi-variate Gaussian, and we can directly read off the

Irrep	Moment	Eigenvalue	Basis
$A_{1u}$	Monopole	$4J_1 + J_2$	$(1, 1, 1, 1, 1, 1)$ / $\sqrt{6}$
$E_u$	Quadrupole	$-2J_1 + J_2$	$(-1, -1, 2, -1, -1, 2)$ / $\sqrt{12}$ $(1, -1, 0, 1, -1, 0)$ / $\sqrt{4}$
$T_{1g}$	Dipole	$-J_2$	$(1, 0, 0, -1, 0, 0)$ / $\sqrt{2}$ $(0, 1, 0, 0, -1, 0)$ / $\sqrt{2}$ $(0, 0, 1, 0, 0, -1)$ / $\sqrt{2}$

TABLE III. Irreps, Eigenvalues and eigenvectors of the interaction matrix for a single tetrahedron, labeled by irreducible representations of  $O_h$ .

correlation functions

$$\mathcal{G}(\{\lambda_i\})_{ij} = \langle S_i^z S_j^z \rangle = [\Lambda + \beta \mathcal{J}]_{ij}^{-1}, \quad (\text{D4})$$

and the self-consistency condition reads  $\mathcal{G}_{ii} = 1$  for all  $i$ . For a system in which every site  $i$  is equivalent by symmetry, the problem simplifies since all  $\lambda_i = \lambda$ . The self-consistency condition can then be simplified to an average over all sites,

$$\frac{1}{N_{\text{sites}}} \text{Tr}[\mathcal{G}(\lambda)] = 1. \quad (\text{D5})$$

In practice this is solved by Fourier transformation to block-diagonalize  $\mathcal{J}$ , then numerically solving the self-consistency equation. In this work we utilize the SCGA to compute the structure factors shown in Fig. 7(b,c), which show excellent agreement with the Monte Carlo calculations.

#### Appendix E: Structure Factors and Neutron Scattering

The neutrons are scattered by the magnetic field produced by the local Ising moments  $\boldsymbol{\mu}_i \propto S_i \hat{z}_i$  of the ions in the lattice. For unpolarized neutrons, the scattering cross section is proportional to

$$S_{\text{unp}}(\mathbf{q}) = \sum_{\mu, \nu} \sum_{\alpha, \beta} (\delta_{\alpha\beta} - \hat{q}^\alpha \hat{q}^\beta) \hat{z}_\mu^\alpha \hat{z}_\nu^\beta \langle S_\mu^z(-\mathbf{q}) S_\nu^z(\mathbf{q}) \rangle, \quad (\text{E1})$$

where the projector arises because the magnetic field is divergence-free. Polarization analysis further refines this cross-section into two channels, denoted spin flip (SF) and non-spin-flip (NSF), referring to filtering the scattered neutrons according to whether they flipped or not. We consider incident neutrons initially polarized in the direction  $\hat{z}_s$ . For each scattering wavevector  $\mathbf{q}$  such that  $\mathbf{q} \perp \hat{z}_s$ , we define a local orthonormal frame  $\{\hat{x}_s, \hat{y}_s, \hat{z}_s\}$ , where  $\hat{x}_s = \hat{q}$  and  $\hat{y}_s = \hat{z}_s \times \hat{x}_s$ . The SF and NSF cross-sections are then proportional to the

following structure factors,

$$S_{\text{SF}}(\mathbf{q}) = \sum_{\mu\nu} (\hat{\mathbf{z}}_\mu \cdot \hat{\mathbf{y}}_s) \langle S_\mu^z(-\mathbf{q}) S_\nu^z(\mathbf{q}) \rangle (\hat{\mathbf{z}}_\mu \cdot \hat{\mathbf{y}}_s),$$

$$S_{\text{NSF}}(\mathbf{q}) = \sum_{\mu\nu} (\hat{\mathbf{z}}_\mu \cdot \hat{\mathbf{z}}_s) \langle S_\mu^z(-\mathbf{q}) S_\nu^z(\mathbf{q}) \rangle (\hat{\mathbf{z}}_\mu \cdot \hat{\mathbf{z}}_s). \quad (\text{E2})$$

which satisfy

$$S_{\text{unp}}(\mathbf{q}) = S_{\text{SF}}(\mathbf{q}) + S_{\text{NSF}}(\mathbf{q}) \quad (\text{E3})$$

## Appendix F: Monte Carlo Simulations

In this Appendix we provide details of the Monte Carlo simulations. Simulations are performed in the 24-site unit cell, for a system of  $L \times L \times L$  unit cells with periodic boundaries.

### 1. Cluster Algorithm for the X-cube Fracton CSL

Otsuka developed a highly efficient cluster algorithm for the simulation of nearest-neighbor pyrochlore spin ice [59], which can straightforwardly be adapted for octochlore spin ice [43]. Here we detail how we adapt this algorithm for the X-cube fracton spin studied in Section V. The algorithm works by a graph decomposition of the partition function, see Ref. [59] for details. The result is a decomposition of any spin configuration into clusters of spins connected by graphs, which may each be flipped independently with 50% probability. Each octahedron is assigned one of a number of graphs  $G$  such that the Boltzmann weight for a spin configurations  $S$  can be expanded as a sum of compatible graph weights

$$e^{-\beta E([S])} \equiv w([S]) = \sum_G \Delta_{S,G} w([G]) \quad (\text{F1})$$

where  $\Delta_{S,G} = 1$  if graph  $G$  is compatible with spin configurations  $S$  and 0 otherwise, and  $w([G])$  are the graph weights. Here,  $[S]$  denotes an equivalence class of spin configurations which are related by a point group transformation, and  $[G]$  denotes an equivalence class of graphs. Each graph equivalence class  $[G]$  must contain all symmetry-equivalent graphs, but may contain multiple graphs which are not related by symmetry. To obtain the graph weights, Eq. (F1) is rewritten as

$$w([S]) = \sum_{[G]} \Gamma_{[S],[G]} w([G]), \quad (\text{F2})$$

where  $\Gamma_{[S],[G]} = \sum_{G \in [G]} \Delta_{S,G}$ . In this form we can see that solving for  $w([G])$  can be done by inverting the matrix  $\Gamma_{[S],[G]}$ , assuming that the number of spin classes  $[S]$  is the same as the number of graph classes  $[G]$ ,

$$w([G]) = \sum_{[S]} \Gamma_{[G],[S]}^{-1} w([S]). \quad (\text{F3})$$

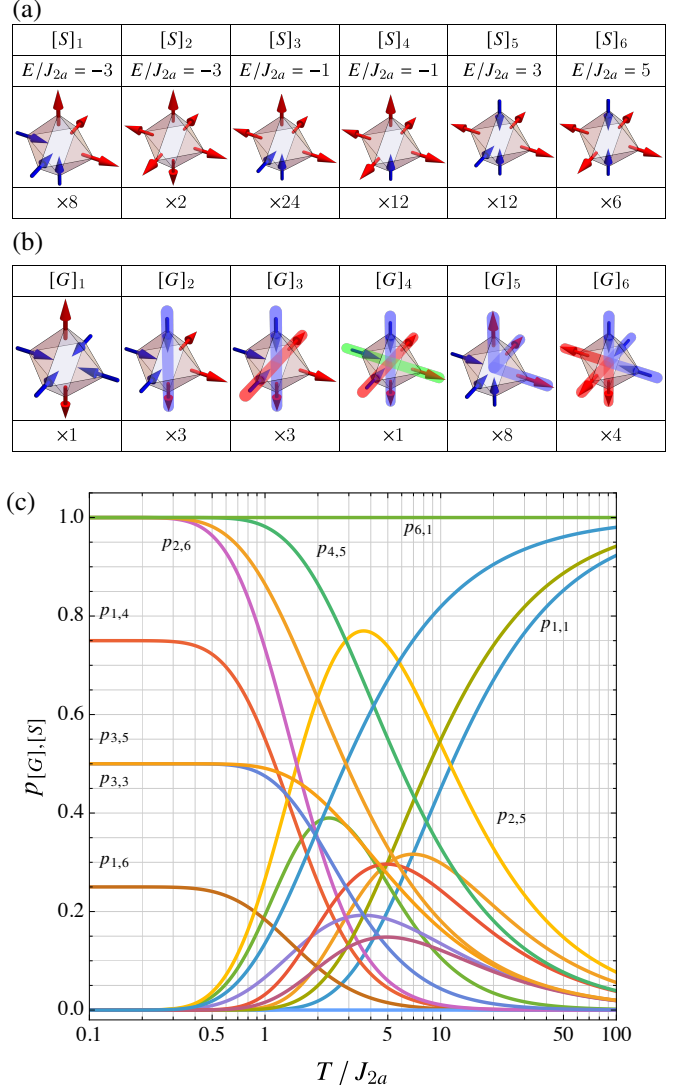


FIG. 12. **Cluster algorithm for the X-cube CSL.** (a) Symmetry classes of single-octahedron spin configurations along with their energies at the X-cube point, and their multiplicities below (64 total states), (b) Symmetry classes of graphs for the X-cube point along with their multiplicities. (c) Probabilities of graph class assignments as a function of temperature,  $p_{[G],[S]} = \sum_{G \in [G]} p(G|S)$ , which is the same for all  $S \in [S]$ .

From these the probabilities for graph assignments are given by [59]

$$p(G|S) = \Delta_{S,G} w([G])/w([S]). \quad (\text{F4})$$

Note that  $\sum_G p(G|S) = 1$  using Eq. (F2). The algorithm works by fixing a spin configuration, applying a random graph  $G$  to every octahedron with probability given by Eq. (F4), identifying the resulting clusters, and flipping each with 50% probability.

The graph types  $[G]$  must be chosen in a way that is compatible with the ground state constraints. In the case of spin ice, the ground state satisfies a zero-divergence constraint and

is therefore a string condensate (where a string connects an in-spin to an out-spin), with no restriction on the geometry of the strings. Thus the graphs should be chosen to pair up in with out spins on each octahedron and their weights  $w(G)$  depend only on the number of “loose ends” of the strings [43]. The graph choices must be modified when moving away from the spin ice point in order for positive weights  $w(G)$  to exist.

For the X-cube point we know that in the ground state only straight strings and 3-in or 3-out “corners” are flippable on a single octahedron. Therefore we choose the graphs accordingly as shown in Fig. 12(b), which contain either straight segments ( $[G]_1$  through  $[G]_4$ ) or three-spin corners ( $[G]_5$  and  $[G]_6$ ). We then compute the coefficients  $\Gamma_{[S],[G]}$ , and compute the corresponding probabilities Eq. (F4), plotted as functions of temperature in Fig. 12(c).

## 2. Finite-Temperature Phase Diagram

In Fig. 1(f) we report critical temperatures  $T_c$  for various angles on the unit-circle parametrization of the intra-octahedral second-nearest-neighbor octochlore Ising phase diagram. Simulations were performed on an  $L = 24$  system with a 6-spin unit cell. A parallel tempering scheme with 100 replicas was employed, with temperature grids centered around the expected  $T_c$  values. Each simulation included  $10^4$  thermalization sweeps, followed by  $10^5$  measurements, with measurements taken every 10 sweeps and parallel tempering swaps performed every 5 sweeps. The critical temperatures  $T_c^{\text{AIAO}}$  and  $T_c^{\text{uni}}$  were identified as the positions of the  $C_V$  peak, accompanied by saturation of the associated order parameter. Whereas the  $T_c^{\text{bi}}$  were extracted from the temperature where the minimal two degenerate eigenvalues (see Fig. 8(b)) split. The resulting  $T_c$  values are plotted on a linear scale as a function of  $\theta$  in Fig. 13. Figure 1(f) of the main text presents the  $T_c$  values on a non-linear scale with radial position:  $r(T/J) = 1 - \tanh(\sqrt{T/10J})$ .

## 3. Thermodynamics

In our Monte Carlo simulations we compute the specific heat from the variance of energy divided by the temperature squared,

$$C_V = \frac{1}{N_B L^3} \frac{\langle E^2 \rangle - \langle E \rangle^2}{T^2}. \quad (\text{F5})$$

Here  $N_B$  is the number of spins in the unit cell simulated (Appendix A). The uncertainties presented in the text are obtained with Jack-knife binning. The entropy per spin is computed by integrating  $C_V/T$

$$S(T) = S(\infty) - \int_T^{T_{\max}} \frac{C_V}{T} dT - \int_{T_{\max}}^{\infty} \frac{C_V}{T} dT, \quad (\text{F6})$$

where  $S(\infty) = \ln 2$  and  $T_{\max}$  is the highest temperature simulated in MC simulations. The integration is performed in two

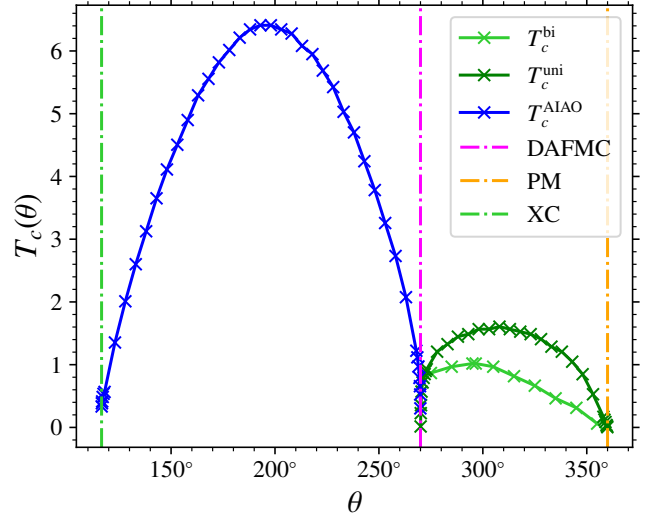


FIG. 13. **Finite-temperature phase boundaries.** Critical temperatures  $T_c(\theta)/J$  for the intra-octahedral second-nearest-neighbor octochlore Ising phase diagram. The couplings are parametrized as  $J_1 = J \cos \theta$  and  $J_{2a} = J \sin \theta$ , normalized to the unit circle. Monte Carlo estimates of  $T_c$  are shown for the ordered phases [all-in-all-out (AIAO), spin-nematic (SN)], with vertical dashed lines indicating special points of interest: the X-cube (XC), decoupled antiferromagnetic chains (DAFMC) and the trivial paramagnet (PM). These values serve as the input for the polar representation of the phase diagram presented in Fig. 1(f) on the non-linear radial scale:  $r(T/J) = 1 - \tanh(\sqrt{T/10J})$ .

parts. The first integral in Eq. (F6) is evaluated with a numerical quadrature routine with the  $C_V$  data presented in Fig. 6. The latter integral approximates  $C_V$  with the high temperature expansion

$$C_V \approx \frac{a}{T^2} + \frac{b}{T^3}, \quad (\text{F7})$$

so that upon fitting the high temperature tail from MC simulations, the second integral of Eq. (F6) evaluates as

$$\int_{T_{\max}}^{\infty} \frac{C_V}{T} dT = \frac{a}{2T_{\max}^2} + \frac{b}{3T_{\max}^3}. \quad (\text{F8})$$

## 4. X-cube Spin Liquid

In Fig. 6(c) and Fig. 7(b,c), we present thermodynamic data of the X-cube CSL discussed in Section V. Cluster algorithm simulations were performed on  $L = 16, 20, 24$  systems (24-site unit cell), initialized from a random configuration. Simulated annealing was employed to cool from  $T_{\max} \rightarrow T_{\min}$  across 40 temperatures for three ranges: (i) logarithmic,  $10^2 J/\sqrt{5} \rightarrow J/\sqrt{5}$ ; (ii) linear,  $2.5J/\sqrt{5} \rightarrow 1.5J/\sqrt{5}$ ; (iii) linear,  $1.46J/\sqrt{5} \rightarrow 0.35J/\sqrt{5}$ . These ranges were chosen to better resolve the  $C_V$  peak. Each temperature grid comprised 1000 simulations, with  $10^4$  thermalization sweeps

followed by 5000 measurements per temperature, sampled every 5 sweeps. This yields a total of  $5 \times 10^6$  measurements per temperature.

In the entropy calculation, the high temperature  $C_V$  data for the  $L = 24$  system presented in Fig. 6 was fitted for  $T \geq 50J$  to Eq. (F7) to obtain

$$a = 7.91 \pm 0.02 \quad b = -31.0 \pm 0.3, \quad (\text{F9})$$

which ultimately yields a high temperature contribution to the entropy

$$\int_{T_{\max}}^{\infty} \frac{C_V}{T} dT = (4.06 \pm 0.01) \times 10^{-4}. \quad (\text{F10})$$

The entropy  $S(T)$  data was then obtained by numerically integrating  $C_V(T)/T$  as described in Eq. (F6). Lastly, we obtain error bars for the complete integral by using a resampling method where we use the jackknife errorbars of  $C_V$  to create  $N_{\text{samp}} = 10^3$  synthetic data sets and perform the process described above to obtain a standard deviation of the resulting entropy curves which is taken to be the error of the entropy.

## 5. Spin Nematic

In Fig. 8, we present thermodynamic data of the spin-nematic model which is diametrically opposite to the fractonic X-cube model in Fig. 1(f) labeled “Fully Packed Fractons”. There are three simulations presented in Fig. 8. The main axes implement single spin flips with simulated annealing which cools a  $L = 20$  (24-site unit cell) system from  $T_{\max} = 4.5/\sqrt{5} \rightarrow T_{\min} = 0.3\sqrt{5}$  with  $N_T = 60$  temperatures. For all temperatures,  $10^4$  thermalization sweeps are performed before  $10^5$  measurements are made after every 7 sweeps of the lattice. The data presented in the insets of Fig. 8(a) are two simulations for each system size,  $L = 16, 20, 24$  using parallel tempering to capture the two specific heat anomalies exhibited in this model. The higher temperature simulation initializes  $N_T = 64$  replicas to a random configuration, and thermalized for  $10^4$  sweeps before recording  $10^6$  samples separated by 5 sweeps. As discussed in Section VI, cooling through  $T_c^{\text{uni}}$  the system undergoes a breaking of rotational symmetry; therefore, to obtain consistent values of  $Q^{\alpha\alpha}$  ( $\alpha \in \{x, y, z\}$ ) at a given temperature below  $T_c^{\text{uni}}$  we initialize all replicas to a configuration that was slowly annealed through the transition for all  $L$ . After initializing  $N_T = 64$  replicas to this configuration the system was thermalized for  $10^4$  sweeps with parallel tempering swaps every 3 sweeps of the lattice, before making  $10^6$  measurements separated by 10 sweeps of the lattice.